Computational Materials Science 250 (2025) 113688

Contents lists available at ScienceDirect

Computational Materials Science

journal homepage: www.elsevier.com/locate/commatsci

Full Length Article

Numerical simulation method for the laser powder bed fusion process by lattice Boltzmann and multi-phase field methods

Sukeharu Nomoto *, Masahiro Kusano, Tomonori Kitashima, Makoto Watanabe

National Institute for Materials Science, 1-2-1 Sengen, Tsukuba, Ibaraki 305-0047, Japan

ARTICLE INFO

Keywords:
Laser powder bed fusion
Modified lattice kinetic scheme
Conserved Allen–Cahn equation
Multi-phase field method
Solidification microstructure evolution
Nickel alloy
MPI and OpenMP

ABSTRACT

The modified lattice kinetic scheme, which is a type of lattice Boltzmann method, was applied to simulate a fluid flow consisting of atmosphere gas and melt liquid with a free surface for the melt pool. The conserved Allen–Cahn equation, which was also transformed to the modified lattice kinetic scheme formulation, was adapted to track the liquid–solid free surface moving dynamics. In addition, a multi-phase field formulation for the modified lattice kinetic scheme of the conserved Allen–Cahn equation was derived for adaptation to a three-phase (gas, liquid and solid) system. Melting and solidification of metal alloy were modelled by a multi-phase field method with consideration of grain interface anisotropy. The thermal equation with a traveling laser beam as heat source was solved by coupling fluid flow and melting / solidification analysis. A highly parallelized computational program was developed by using the Message-Passing Interface (MPI) and Open Multi-Processing (OpenMP) hybrid method. A three-dimensional model of powder bed fusion additive manufacturing of Ni alloy consisting of atmosphere gas, a base plate, and powder regions was built. Simulation was conducted using a laser beam traveling a passage. The pores generated from the initial space between the powder particles and transformed in the liquid by flow convection were shown. It was confirmed that the present numerical framework provided a high speed and robust method for large scale modelling of the powder bed fusion process from melting to solidification microstructure evolution.

1. Introduction

Additive manufacturing (AM) is now a common engineering method for the production of solid parts by adding material layer-by-layer [1,2,3]. AM has the advantages of consuming smaller amounts of material and allowing fabrication of small lots. There are many kinds of AM, each with a different fabrication mechanism. Examples include wire arc additive manufacturing (WAAM) [4,5,6], directed energy deposition (DED) using wire or powder [7,8,9], binder jet three-dimensional (3D) printing (BJ3DP) [10,11] and powder bed fusion (PBF) using a laser or an electron beam. PBF has the advantage that it can produce complex 3D metallic parts through rapid cycles of melting and solidification of selected metal alloy powder granules [12,13,14,15]. Furthermore, it provides better surface quality and dimensional accuracy than the other methods. Laser powder bed fusion (LPBF) is more widely used in the manufacturing industry than electron PBF due to the lower operational cost of LPBF. The research and discussion in the present study is focused on the LPBF process.

In the LPBF process, a high-power laser spot with a small diameter traveling at high velocity generates a rapid change of temperature distribution, with a maximum cooling rate and high temperature gradient of approximately 10^5-10^7 K/s and 10^6-10^8 K/m [16,17,18,19], respectively. This chaotic temperature condition tends to give rise to some defects, such as distortion of parts, unfused powder particles, surface and internal cracks, and pores [20,21,22]. In the LPBF process, not only the many process parameters of laser power, beam diameter, energy density distribution, traveling velocity, hatch space, scan pattern, powder bed thickness and support shape, but also powder properties of particle size and its distribution, flowability, packed density, and mechanical and chemical properties affect the grain microstructure formation and the defect generation [23]. To date, however, no simple design model has been established to replicate the precise process conditions and reduce the defects. Instead, the process conditions are designed mainly by referring to a database established under repeated experimental measurements. Recently, some attempts have been made to introduce a machine learning approach to reduce the number of experiments [24,25,26].

Some numerical approaches for the LPBF process have been

---

* Corresponding author.
E-mail address: NOMOTO.Sukeharu@nims.go.jp (S. Nomoto).

https://doi.org/10.1016/j.commatsci.2025.113688
Received 30 October 2024; Received in revised form 10 January 2025; Accepted 11 January 2025

attempted to analyze the multi-physics behavior, temporal thermal distribution, powder melting, luck of fusion, melt pool flow, pore generation, solidification microstructure and solute segregation. The finite element method (FEM) is very frequently applied to thermal analysis to reduce the required calculation time [27,28,29]. Residual stress field and deformation are estimated from the temporal temperature distribution obtained in the thermal analysis [30,31]. Numerous studies using computational fluid dynamics (CFD) to analyze melt pool generation, flow behavior with free surface movement, luck of fusion and keyhole pore generation, have also been reported [32,33,34,35]. The solidification microstructure evolution weakly coupling with CFD analysis is demonstrated by using a cellular automaton (CA) [36,37]. The phase field method (PFM) is also applied to the solidification microstructure evolution by coupling with thermal analysis [38,39] or CFD analysis [40]. PFM has the advantage by comparing with CA, by providing rapid solidification microstructure evolution in thermodynamically non-equilibrium condition of LPBF process [41,42]. However, in the CFD model for LPBF, solids are generally assumed to be high-viscosity liquids. As this assumption, solidification microstructure evolution is weakly coupling with CA or CFD analyses. Furthermore, in our experience, the execution of CFD analysis for LPBF is very time consuming, particularly for the 3D model [43]. Some numerical methodology for solidification microstructure evolution fully coupled with CFD analysis is needed to reduce the total simulation time and increase reliability.

The Lattice Boltzmann method (LBM) is now generally well known as a method with low consumption of calculation time and high numerical stability. LBM can be adapted to the multi-phase flow [44,45]. Attempts to apply LBM to analysis of the LPBF process have been reported [46,47]. In the CFD method, the free surface movement is usually tracked by introducing the volume of fluid (VOF) method [48]. The variable of the liquid/gas volume ratio in the cell is defined in the CFD method. A similar definition of liquid/gas ratio in the cell has been reported to be adapted to LBM for the LPBF process flow [49]. In this case, flow velocity in the gas region is usually not solved in order to maintain numerical stability for the surface tracking. Neglecting the gas flow field also neglects the effects of the liquid/gas density and viscosity value ratios. These omissions also improve the numerical stability. However, the above simplification is considered to afford an insufficient approximation of the practical flow behavior. On the other hand, methods with sophisticated functions are available to track the free surface by expressing Cahn–Hilliard (CH) [50,51,52] or conserved Allen–Cahn (CAC) equations [53,54]. These tracking equations permit tracking of the free surface movement with consideration of the gas flow field. It is confirmed that the CAC equation has higher accuracy for maintaining small bubble volume than the CH equation, because it contains a fourth order differentiation term with larger numerical error [55]. Nevertheless, there has been no large, 3D LPBF process simulation using LBM with the free surface movement tracked by Cahn–Hilliard (CH) or conserved Allen–Cahn (CAC) equations.

Suzuki and Inamuro proposed a kind of LBM, the modified lattice kinetic scheme (MLKS), which has the capability to simulate liquid/gas flow with free surface tracking under condition of large differences between gas/liquid density and viscosity [56]. They demonstrated a crown droplet splashing flow simulated by MLKS for flow and CH equation [57]. On the other hand, in the LPBF process, the system contains three phases—solid, gas and liquid—after solid melting with a triple phase boundary point. Multi-phase treatment for the liquid/gas interface is necessary in the ripple point. Fortunately, the CAC equation was extended to a multi-phase formulation by Lee and Kim [58]. In this study, this extended formulation is called the multi-phase conserved Allen–Cahn (MPCAC) equation, and it is transformed to the MLKS formulation in order to allow efficient coupling with the MLKS flow calculations.

Also in this study, the standard multi-phase field method (MPFM) is adapted for melting and solidification microstructure evolution in the solid/liquid boundary region [59]. In addition, MLKS and MPCAC are adapted for liquid/gas flow and the free surface movement, respectively. The phase order variable distributions at each discrete time are shared between MPCAC and MPFM calculations in the following manner. In the MLKS flow calculation of MPCAC liquid/gas interface movement, the solid distribution is fixed. Conversely, in the MPFM calculation of melting and solidification at each discrete time, the gas distribution is fixed. These calculations are alternately repeated at each time point. The liquid/gas flow, melting and multi-grain solidification microstructure calculations are then synchronized with the temporal temperature distribution calculated by thermal analysis in the LPBF model. An in-house computational program solving these equations is developed by using MPI and OpenMP hybrid parallelization to accelerate the reduction in the consumption of calculation time. As a result, 3D simulation for the LPBF process in achieved, including the temporal temperature distribution heated by laser beam traveling, metal powder and base plate melting, liquid/gas flow with free surface movement and multi-grain solidification microstructure evolution.

2. Numerical method

2.1. Modified lattice kinetic scheme for Gas–Liquid flow

The modified lattice kinetic scheme (MLKS) was proposed by Suzuki and Inamuro as a kind of lattice Boltzmann method (LBM) [56]. MLKS was developed to simulate a liquid–gas mixture flow with high numerical stability under high density ratio and high viscosity ratio conditions with free surface moving motion. The standard LBM does not treat the pressure equation directly. It permits quasi-compression. On the other hand, MLKS must solve the following iterative pressure equation, in which constant densities for liquid and gas phases are defined:

$$p(\boldsymbol{x},t+\Delta t)=p(\boldsymbol{x},t)+\frac{\omega(\boldsymbol{x},t)}{3}\sum\nolimits_{i=1}^{15}\left[\Delta P_i+g_i^{\mathrm{eq}}(\boldsymbol{x}-\boldsymbol{c}_i\Delta x,t)\right] \tag{1}$$

where $p(\boldsymbol{x},t)$ is pressure at time t, g_i^{eq} is the equilibrium distribution function, $\boldsymbol{c}_i$ is the discretized particle velocity vector, and Δx is the lattice spacing of LBM. Note that all variables are defined as dimensionless in MLKS just as for LBM. The characteristic values for dimensionless variables must be carefully selected to maintain the numerical stability. ω is the over-relaxation parameter and is defined as follows:

$$\omega(\boldsymbol{x},t)=\frac{\rho(\boldsymbol{x},t)-\rho_G}{\rho_L-\rho_G}(\omega_{max}-\rho_G)+\rho_G,\rho_G\leq\omega_{max}\leq\rho_L \tag{2}$$

ΔP_i in Eq. (1) is provided as

$$\Delta P_i=\frac{3}{2}E_i\left[\frac{1}{\rho(\boldsymbol{x}-\boldsymbol{c}_i\Delta t,t)}+\frac{1}{\rho(\boldsymbol{x},t)}\right][p(\boldsymbol{x}-\boldsymbol{c}_i\Delta x)-p(\boldsymbol{x})] \tag{3}$$

where E_i is the weight of the LBM definition. In this study, the 3D 15-velocity model (D3Q15), $i=1\sim15$, is applied to the MLKS formulations [60]. $\boldsymbol{c}_i$ and E_i are summarized in Table 1. ρ in Eq. (2) is density and is assumed by linear interpolation as

$$\rho=\phi(\rho_{\mathrm{G}}-\rho_{\mathrm{L}})+\rho_{\mathrm{L}} \tag{4}$$

where ρ_{L} and ρ_{G} are the liquid and gas densities, respectively. ϕ is a phase order variable of the gas phase in the interface region of the free

Table 1
Three-dimensional 15-velocity model (D3Q15 model).

i	$\boldsymbol{c}_i$	E_i
1	$(0,0,0)$	$\frac{2}{9}$
2, 3, 4, 5, 6, 7	$(\pm1,0,0),(0,\pm1,0),(0,0,\pm1)$	$\frac{1}{9}$
8, 9, 10, 11, 12, 13, 14, 15	$(\pm1,\pm1,\pm1)$	$\frac{1}{72}$

surface that is defined as $0 \le \phi \le 1$. $\phi = 0$ and $\phi = 1$ indicate liquid and gas matrixes, respectively. $0 < \phi < 1$ represents the interface region between liquid and gas phases. The ϕ distribution is derived by the conserved Allen–Cahn equation [61], which is described later. In this study, it is defined that $\rho_{\mathrm{G}} = 1$ and $\rho_{\mathrm{L}} >> 1$. The equilibrium distribution function of MLKS, g_i^{eq}, in Eq. (1) is defined using the same formulation as the standard LBM one:

$$g_i^{\mathrm{eq}} = E_i\left[3\boldsymbol{c}_i\cdot\boldsymbol{u} + \frac{9}{2}(\boldsymbol{c}_i\cdot\boldsymbol{u})^2 - \frac{3}{2}\boldsymbol{u}^2\right] \tag{5}$$

where $\boldsymbol{u}$ is the flow velocity vector.

Equation (1) leads to the Poisson equation for pressure under the condition of spatially changing density by the following procedure. First, substitution of the temporal Taylor expansion up to the first derivative term of $p(\boldsymbol{x}, t+\Delta x)$ into Eq. (1) gives

$$\Delta t\frac{\partial p}{\partial t} = \frac{\omega}{3}\sum_{i=1}^{15}\left[\Delta P_i + g_i^{\mathrm{eq}}(\boldsymbol{x} - \boldsymbol{c}_i\Delta x, t)\right] + O\left[(\Delta t)^2\right] \tag{6}$$

where the description $(\boldsymbol{x}, t)$ is omitted. Next, spatial Tayler expansion up to the second derivative term for $\boldsymbol{x} - \boldsymbol{c}_i\Delta x$ is applied to $\rho(\boldsymbol{x} - \boldsymbol{c}_i\Delta t, t)$ and $p(\boldsymbol{x} - \boldsymbol{c}_i\Delta x)$ in Eq. (3), giving the following equation:

$$\Delta P_i = \frac{3}{2}E_i\left[-\Delta x c_{i\beta}\frac{2}{\rho}\frac{\partial p}{\partial x_\beta} + (\Delta x)^2 c_{i\beta}c_{i\gamma}\left\{\frac{\partial(1/\rho)}{\partial x_\beta}\frac{\partial p}{\partial x_\gamma} + \frac{1}{\rho}\frac{\partial^2 p}{\partial x_\beta\partial x_\gamma}\right\}\right] + O\left[(\Delta x)^3\right] \tag{7}$$

Spatial Tayler expansion of $(\boldsymbol{x} - \boldsymbol{c}_i\Delta x, t)$ is also applied to $g_i^{\mathrm{eq}}(\boldsymbol{x} - \boldsymbol{c}_i\Delta x, t)$ by using Eq.(5), which leads to the following:

$$\begin{aligned} g_i^{\mathrm{eq}}(\boldsymbol{x} - \boldsymbol{c}_i\Delta x, t) = E_i\Bigg[&3c_{i\alpha}u_\alpha + \frac{9}{2}c_{i\alpha}c_{i\gamma}u_\alpha u_\gamma - \frac{3}{2}u_\alpha u_\alpha - \Delta x c_{i\beta}\left\{3c_{i\alpha}\frac{\partial u_\alpha}{\partial x_\beta}\right. \\ &+ \frac{9}{2}c_{i\alpha}c_{i\gamma}\frac{\partial}{\partial x_\beta}(u_\alpha u_\gamma) \\ &\left.- \frac{3}{2}\frac{\partial}{\partial x_\beta}(u_\alpha u_\alpha)\right\} + \frac{1}{2}(\Delta x)^2 c_{i\beta}c_{i\gamma}\left\{3c_{i\alpha}\frac{\partial^2 u_\alpha}{\partial x_\beta\partial x_\gamma}\right. \\ &\left.+ \frac{9}{2}c_{i\alpha}c_{i\delta}\frac{\partial^2}{\partial x_\beta\partial x_\gamma}(u_\alpha u_\delta) - \frac{3}{2}\frac{\partial^2}{\partial x_\beta\partial x_\gamma}(u_\alpha u_\alpha)\right\}\Bigg] + O\left[(\Delta x)^3\right] \end{aligned} \tag{8}$$

Summation of Eq. (8) provides

$$\sum_{i=1}^{15} g_i^{\mathrm{eq}}(\boldsymbol{x} - \boldsymbol{c}_i\Delta x, t) = -\Delta x\frac{\partial u_\alpha}{\partial x_\alpha} + \frac{1}{2}(\Delta x)^2\frac{\partial^2}{\partial x_\alpha\partial x_\beta}(u_\alpha u_\beta) \tag{9}$$

Summation of Eq. (7) leads to,

$$\sum_{i=1}^{15}\Delta P_i = \frac{1}{2}(\Delta x)^2\frac{\partial}{\partial x_\alpha}\left(\frac{1}{\rho}\frac{\partial p}{\partial x_\alpha}\right) \tag{10}$$

Substituting Eqs. (9) and (10) into Eq. (6) results in

$$\Delta t\frac{\partial p}{\partial t} = \frac{\omega}{3}\left[-\Delta x\frac{\partial u_\alpha}{\partial x_\alpha} + \frac{1}{2}(\Delta x)^2\left\{\frac{\partial}{\partial x_\alpha}\left(\frac{1}{\rho}\frac{\partial p}{\partial x_\alpha}\right) + \frac{\partial^2}{\partial x_\alpha\partial x_\beta}(u_\alpha u_\beta)\right\}\right] \tag{11}$$

Under condition of converged pressure, which can be assumed as $\frac{\partial p}{\partial t} = 0$, Eq. (11) provides the following two relations:

$$\frac{\partial u_\alpha}{\partial x_\alpha} = 0 \tag{12}$$

$$\frac{\partial}{\partial x_\alpha}\left(\frac{1}{\rho}\frac{\partial p}{\partial x_\alpha}\right) = -\frac{\partial^2}{\partial x_\alpha\partial x_\beta}(u_\alpha u_\beta) \tag{13}$$

Equations (12) and (13) show the continuity condition of incompressible flow and Poisson equation for pressure, respectively. The iteration scheme for pressure, Eq. (1), has similarity to the computational fluid dynamics (CFD) schemes, and the maker and cell (MAC) or semi-implicit method for pressure linked equation (SIMPLE) methods. However, the MAC or SIMPLE schemes expend much computational cost to solve the pressure equation due to the huge iteration number for convergence because the parabolic partial differential equation of Eq. (13) is directly solved by the finite difference method (FDM), finite volume method (FVM) or finite element method (FEM). On other hand, in MLKS, Eq. (1) is usually rapidly converged by fewer than five iterations. MLKS has a greater advantage for fast computation than the CFD method.

The time evolution of the flow velocity vector in LBM is determined as

$$\rho\boldsymbol{u} = \sum_{i=1}^{15}\boldsymbol{c}_i f_i^{eq} \tag{14}$$

where f_i^{eq} is the equilibrium velocity distribution function of LBM. On the other hand, in MLKS, the flow velocity is provided as follows by using ΔP_i and g_i^{eq}:

$$\begin{aligned} \boldsymbol{u}(\boldsymbol{x}, t+\Delta t) = \sum_{i=1}^{15}\boldsymbol{c}_i\big\{&\Delta P_i(\boldsymbol{x}, t+\Delta t) + g_i^{eq}(\boldsymbol{x} - \boldsymbol{c}_i\Delta x, t) \\ &+ 3A_u E_i c_{i\beta}\left[u_\beta(\boldsymbol{x}, t) - u_\beta(\boldsymbol{x} - \boldsymbol{c}_i\Delta x, t)\right] + 3A_u E_i c_{i\beta}V_\beta(\boldsymbol{x}, t)\big\} \\ &+ \frac{1}{\rho(\boldsymbol{x}, t)}\boldsymbol{F}_{SV}\Delta x + \frac{1}{\rho(\boldsymbol{x}, t)}\boldsymbol{F}_{rcl}\Delta x + \frac{1}{\rho(\boldsymbol{x}, t)}\boldsymbol{F}_{buoy}\Delta x \end{aligned} \tag{15}$$

where A_u is a relaxation coefficient, which is related with viscosity μ as follows:

$$\mu = \frac{1}{6}\rho(1 - A_u)\Delta x \tag{16}$$

where μ is defined using the viscosities of gas and liquid, μ_{G} and μ_{L}, respectively, as the same linearly interpolated formulation as in Eq. (4),

$$\mu = \phi(\mu_{\mathrm{G}} - \mu_{\mathrm{L}}) + \mu_{\mathrm{L}} \tag{17}$$

V_β in Eq. (15) is defined as

$$V_\beta = \frac{1}{\rho}\frac{\partial\mu}{\partial x_\beta}\left(\frac{\partial u_\alpha}{\partial x_\beta} + \frac{\partial u_\beta}{\partial x_\alpha}\right)\Delta x \tag{18}$$

This term presents the viscosity change at the interface of gas and liquid. The terms $\boldsymbol{F}_{\mathrm{SV}}$ and $\boldsymbol{F}_{\mathrm{rcl}}$ in Eq. (15) are the external force per unit volume in the gas–liquid interface region for the interfacial tension σ and the volumetric force transformed from the recoil pressure p_{rcl} caused by evaporation of metal liquid in the gas–liquid interface region, respectively. A continuous surface model [62] is applied to the transformation from the force per unit area to the volumetric force vector in the interface region between high differences in gas and liquid densities as [54],

$$\begin{cases} \mathbf{F}_{\mathrm{SV}} = \sigma_{\mathrm{GL}}\bullet\chi\bullet\dfrac{\nabla\rho(\boldsymbol{x}, t)}{\rho_{\mathrm{L}} - \rho_{\mathrm{G}}}\cdot\dfrac{\rho(\boldsymbol{x}, t)}{(\rho_{\mathrm{L}} + \rho_{\mathrm{G}})/2} + \dfrac{d\sigma_{\mathrm{GL}}}{dT}\left[\nabla T - (\boldsymbol{n}\bullet\nabla T)\boldsymbol{n}\right]\bullet\dfrac{|\nabla\rho(\boldsymbol{x}, t)|}{\rho_{\mathrm{L}} - \rho_{\mathrm{G}}}\cdot\dfrac{\rho(\boldsymbol{x}, t)}{(\rho_{\mathrm{L}} + \rho_{\mathrm{G}})/2}, \\ \mathbf{F}_{\mathrm{rcl}} = p_{\mathrm{rcl}}\bullet\dfrac{\nabla\rho(\boldsymbol{x}, t)}{\rho_{\mathrm{L}} - \rho_{\mathrm{G}}}\cdot\dfrac{\rho(\boldsymbol{x}, t)}{(\rho_{\mathrm{L}} + \rho_{\mathrm{G}})/2}, \end{cases} \tag{19}$$

where $\boldsymbol{n}$ is the normal unit vector in the interface through the density gradient,

$$\boldsymbol{n} := \frac{\nabla\rho(\boldsymbol{x},t)}{|\nabla\rho(\boldsymbol{x},t)|} \tag{20}$$

and χ is the interface curvature expressed as

$$\chi = -\nabla \bullet \boldsymbol{n}(\boldsymbol{x},t) \tag{21}$$

The second term of $\mathbf{F}_{\mathrm{SV}}$ in Eq. (19) is the tangential effect of σ_{GL}, where temperature dependency is considered for σ_{GL} to include the effect of Marangoni convection in this study as follows:

$$\sigma_{GL} = \sigma_0 + \xi_{Mar}(T - T_M) \tag{22}$$

where σ_0 is the reference interface energy on the gas–liquid interface, $\xi_{Mar} := \frac{d\sigma_{GL}}{dT}$ is the Marangoni coefficient and T_{M} is the melting temperature. In Eq. (19), the following recoil pressure p_{rcl} model proposed by Anisimov is employed [63,64]:

$$p_{prc} = \frac{1+\beta_R}{2}p_0\cdot exp\left[\frac{L_v M_{SLD}}{RT_{vap}}\left(1-\frac{T_{vap}}{T}\right)\right], T \geq T_{vap} \tag{23}$$

where β_{R} is the vaporization ratio, M_{SLD} is the molar mass of metal alloy, R is a gas constant, and p_0 is the non-dimensional atmospheric pressure, which is defined by $\widehat{p}_0/(\rho_G c^2)$. L_{v} is the latent heat of vaporization and T_{vap} is vaporization temperature. It is noted that the vapor flow discontinuities and expansion from the liquid phase to ambient gas are not resolved in this study.

The last term on the right hand side of Eq. (15), $\boldsymbol{F}_{\mathrm{buoy}}$, is the volumetric buoyancy force and determined as:

$$\boldsymbol{F}_{buoy} = g_k[\beta_G\rho_G\phi + \beta_L\rho_L(1-\phi)](T-T_M) - (\rho-\rho_G)g_k \tag{24}$$

The first and second terms show the Boussinesq approximation for the gravity effect of weakly changing density in the gas and liquid phases, respectively, where g_k is the gravity vector, β_{G} and β_L are the bulk modulus values of the gas and liquid phases, respectively, T is temperature and T_M is melting temperature. The third term is the buoyant force caused by the density difference between gas and liquid.

Equation (15) can be transformed to the Navier–Stokes equation in the same manner as shown for the pressure equation. Tayler expansion is applied to $t+\Delta t$ and $\boldsymbol{x}-\boldsymbol{c}_i\Delta x$ up to the first and the second orders, respectively, for the terms $\boldsymbol{u}(\boldsymbol{x},t+\Delta t)$, $\Delta P_i(\boldsymbol{x},t+\Delta t)$, $g_i^{eq}(\boldsymbol{x}-\boldsymbol{c}_i\Delta x,t)$ and $\boldsymbol{u}(\boldsymbol{x}-\boldsymbol{c}_i\Delta x,t)$ in Eq. (15). The expansion of $g_i^{eq}(\boldsymbol{x}-\boldsymbol{c}_i\Delta x,t)$ has already been presented above, in Eq. (8). $\Delta P_i(\boldsymbol{x},t)$ appears in Eq. (7). Taking the Tayler expansion of $\Delta P_i(\boldsymbol{x},t+\Delta t)$ for time leads to

$$\Delta P_i(\boldsymbol{x},t+\Delta t) = \Delta P_i + \Delta t\frac{\partial(\Delta P_i)}{\partial t} \tag{25}$$

where ΔP_i is the first order of Δx as shown in Eq. (7). Note that $\Delta t = \mathrm{Sh}\Delta x$, in which Sh is the Strouhal number defined by $\mathrm{Sh} = \widehat{L}/(\widehat{t_0}\widehat{c}) = \widehat{U}/\widehat{c}$, where $\widehat{L}$ is the characteristic length, $\widehat{t_0}$ the characteristic time, $\widehat{U}$ the characteristic velocity and $\widehat{c}$ the characteristic particle velocity. As Sh has a value depend on the order of the nondimensional grid width, $\mathrm{Sh} = O(\Delta x)$, the second term of Eq. (25) can be neglected because it is the third order of Δx, $O\left[(\Delta x)^3\right]$

$$\Delta P_i(\boldsymbol{x},t+\Delta t) = \Delta P_i(\boldsymbol{x},t) = \frac{3}{2}E_i\left[-\Delta x c_{i\beta}\frac{2}{\rho}\frac{\partial p}{\partial x_\beta} + (\Delta x)^2 c_{i\beta}c_{i\gamma}\left\{\frac{\partial(1/\rho)}{\partial x_\beta}\frac{\partial p}{\partial x_\gamma} + \frac{1}{\rho}\frac{\partial^2 p}{\partial x_\beta\partial x_\gamma}\right\}\right] + O\left[(\Delta x)^3\right] \tag{26}$$

Execution of summation for the first term on the right-hand side of Eq. (26) by using Eq. (7) with consideration for Eq. (26) results in

$$\sum\nolimits_{i=1}^{15} c_{i\alpha}\Delta P_i(\boldsymbol{x},t+\Delta t) = -\Delta x\frac{1}{\rho}\frac{\partial p}{\partial x_\alpha} \tag{27}$$

By substituting Eq. (8), the second term on the right-hand side of Eq. (15) becomes

$$\sum\nolimits_{i=1}^{15} c_{i\alpha}g_i^{\mathrm{eq}}(\boldsymbol{x}-\boldsymbol{c}_i\Delta x,t) = u_\alpha - \Delta x\frac{\partial}{\partial x_\beta}(u_\alpha u_\beta) + \frac{1}{6}(\Delta x)^2\left(\frac{\partial^2 u_\alpha}{\partial x_\beta^2} + 2\frac{\partial}{\partial x_\alpha}\frac{\partial u_\beta}{\partial x_\beta}\right) \tag{28}$$

Substituting Eqs. (18), (27) and (28), $\boldsymbol{u}(\boldsymbol{x},t+\Delta t) = \boldsymbol{u}(\boldsymbol{x},t) + \Delta t\frac{\partial\boldsymbol{u}}{\partial t}$ and $u_\beta(\boldsymbol{x}-\boldsymbol{c}_i\Delta x,t) = u_\beta(\boldsymbol{x},t) - \Delta x c_{i\gamma}\frac{\partial u_\beta}{\partial x_\gamma} + \frac{1}{2}(\Delta x)^2 c_{i\gamma}c_{i\delta}\frac{\partial^2 u_\beta}{\partial x_\gamma\partial x_\delta}$ into Eq. (15) leads to

$$\begin{aligned}\Delta t\frac{\partial\boldsymbol{u}}{\partial t} + \frac{1}{\rho}\boldsymbol{F}_{buoy}\Delta x = &-\Delta x\frac{1}{\rho}\frac{\partial p}{\partial x_\alpha} - \Delta x\frac{\partial}{\partial x_\beta}(u_\alpha u_\beta) + \frac{1}{6}(\Delta x)^2\left(\frac{\partial^2 u_\alpha}{\partial x_\beta^2} + 2\frac{\partial}{\partial x_\alpha}\frac{\partial u_\beta}{\partial x_\beta}\right)\\ &-\frac{1}{6}A_u(\Delta x)^2\left(\frac{\partial^2 u_\alpha}{\partial x_\beta^2} + 2\frac{\partial}{\partial x_\alpha}\frac{\partial u_\beta}{\partial x_\beta}\right) + \frac{1}{\rho}\frac{\partial\mu}{\partial x_\beta}\left(\frac{\partial u_\alpha}{\partial x_\beta} + \frac{\partial u_\beta}{\partial x_\alpha}\right)\Delta x\\ &+\frac{1}{\rho}\boldsymbol{F}_{SV}\Delta x + \frac{1}{\rho}\boldsymbol{F}_{rcl}\Delta x + \frac{1}{\rho}\boldsymbol{F}_{buoy}\Delta x\end{aligned} \tag{29}$$

Dividing both sides by Δx using the relation $\Delta t = \mathrm{Sh}\Delta x$ results in

$$\begin{aligned}Sh\frac{\partial\boldsymbol{u}}{\partial t} + \frac{\partial}{\partial x_\beta}(u_\alpha u_\beta) = &-\frac{1}{\rho}\frac{\partial p}{\partial x_\alpha} + \frac{1}{6}(1-A_u)\Delta x\left(\frac{\partial^2 u_\alpha}{\partial x_\beta^2} + 2\frac{\partial}{\partial x_\alpha}\frac{\partial u_\beta}{\partial x_\beta}\right)\\ &+\frac{1}{\rho}\frac{\partial\mu}{\partial x_\beta}\left(\frac{\partial u_\alpha}{\partial x_\beta} + \frac{\partial u_\beta}{\partial x_\alpha}\right) + \frac{1}{\rho}\boldsymbol{F}_{SV} + \frac{1}{\rho}\boldsymbol{F}_{rcl} + \frac{1}{\rho}\boldsymbol{F}_{buoy}\end{aligned} \tag{30}$$

Applying the relation between the relaxation coefficient A_u and viscosity μ to Eq. (30) gives

$$\begin{aligned}Sh\frac{\partial\boldsymbol{u}}{\partial t} + \frac{\partial}{\partial x_\beta}(u_\alpha u_\beta) = &-\frac{1}{\rho}\frac{\partial p}{\partial x_\alpha} + \frac{\mu}{\rho}\left(\frac{\partial^2 u_\alpha}{\partial x_\beta^2} + 2\frac{\partial}{\partial x_\alpha}\frac{\partial u_\beta}{\partial x_\beta}\right)\\ &+\frac{1}{\rho}\frac{\partial\mu}{\partial x_\beta}\left(\frac{\partial u_\alpha}{\partial x_\beta} + \frac{\partial u_\beta}{\partial x_\alpha}\right) + \frac{1}{\rho}\boldsymbol{F}_{SV} + \frac{1}{\rho}\boldsymbol{F}_{rcl} + \frac{1}{\rho}\boldsymbol{F}_{buoy}\end{aligned} \tag{31}$$

Applying $\frac{\partial^2 u_\alpha}{\partial x_\beta^2} + 2\frac{\partial}{\partial x_\alpha}\frac{\partial u_\beta}{\partial x_\beta} = \frac{\partial}{\partial x_\beta}\left(\frac{\partial u_\alpha}{\partial x_\beta} + \frac{\partial u_\beta}{\partial x_\alpha}\right) + \frac{\partial}{\partial x_\beta}\frac{\partial u_\beta}{\partial x_\beta}$ into Eq. (31) provides the compressible Navier–Stokes equation:

$$\begin{aligned}Sh\frac{\partial\boldsymbol{u}}{\partial t} + \frac{\partial}{\partial x_\beta}(u_\alpha u_\beta) = &-\frac{1}{\rho}\frac{\partial p}{\partial x_\alpha} + \frac{1}{\rho}\frac{\partial}{\partial x_\beta}\left[\mu\left(\frac{\partial u_\alpha}{\partial x_\beta}\right.\right.\\ &\left.\left.+\frac{\partial u_\beta}{\partial x_\alpha}\right)\right] + \frac{\mu}{\rho}\frac{\partial}{\partial x_\beta}\frac{\partial u_\beta}{\partial x_\beta} + \frac{1}{\rho}\boldsymbol{F}_{SV} + \frac{1}{\rho}\boldsymbol{F}_{rcl} + \frac{1}{\rho}\boldsymbol{F}_{buoy}\end{aligned} \tag{32}$$

Finally, adapting the continuity condition, Eq. (12), to Eq. (32) results in the incompressible Navier–Stokes equation:

$$Sh\frac{\partial\boldsymbol{u}}{\partial t} + u_\beta\frac{\partial u_\alpha}{\partial x_\beta} = -\frac{1}{\rho}\frac{\partial p}{\partial x_\alpha} + \frac{1}{\rho}\frac{\partial}{\partial x_\beta}\left[\mu\left(\frac{\partial u_\alpha}{\partial x_\beta} + \frac{\partial u_\beta}{\partial x_\alpha}\right)\right] + \frac{1}{\rho}\boldsymbol{F}_{SV} + \frac{1}{\rho}\boldsymbol{F}_{rcl} + \frac{1}{\rho}\boldsymbol{F}_{buoy} \tag{33}$$

The total volume of atmosphere gas in the LPBF model of this study is assumed to be maintained while the powder and base plate of metal alloy are melted by the traveling laser spot and the molten alloy solidifies after the laser spot passes. The gas–liquid interface moves with the melt pool flow generated by the forces $\boldsymbol{F}_{SV}$, $\boldsymbol{F}_{\mathrm{rcl}}$ and $\boldsymbol{F}_{buoy}$, as shown in Eq. (33). Many previous studies simulating PBF by using LBM do not deal with gas flow because the gas–liquid interface tracking tends to be more stable than treatment of both the gas and liquid flows [55]. As shown by the numerical procedures above, some gas–liquid interface tracking method is needed. Now, there are two capable equations to track interface movement by coupling MLKS. One is the Cahn–Hilliard equation [50,51,52]. The other is the conserved Allen–Cahn equation [53,54]. The former method has a disadvantage that bubble of small diameter tends to numerical disappear because its equation contains forth derivative. In this study, the conserved Allen–Cahn equation is employed to track gas–liquid interface order ϕ distribution.

The conserved Allen–Cahn (CAC) equation is expressed as follows:

$$\mathrm{Sh}\frac{\partial\phi}{\partial t}+\frac{\partial}{\partial x_\alpha}(u_\alpha\phi)=\frac{\partial}{\partial x_\alpha}\left\{M_\phi\left[1-\frac{4}{|\nabla\phi|}\frac{4\phi(1-\phi)}{W}\right]\frac{\partial\phi}{\partial x_\alpha}\right\} \tag{34}$$

The one-dimensional static solution of Eq. Eq 34 is promptly obtained as

$$\phi=\frac{1}{2}\left[1-tanh\left(\frac{2}{W}x\right)\right] \tag{35}$$

From this solution, it is understood that Eq. (34) is a kind of phase-field equation for ϕ, in which double well potential is employed for the energy barrier. The second term in the bracket on the right-hand side of Eq. (34) operates by conserving the gas–liquid fraction ratio by eliminating the curvature effect. M_ϕ is the interface mobility parameter. W is a parameter related to the interface thickness. The MLKS formulation for Eq. (34) was obtained as follows [56]:

$$\phi(\boldsymbol{x},t+\Delta t)=\sum\nolimits_{i=1}^{N}\left\{f_i^{eq}(\boldsymbol{x}-\boldsymbol{c}_i\Delta t,t)+AE_i[\phi(\boldsymbol{x},t)-\phi(\boldsymbol{x}-\boldsymbol{c}_i\Delta t,t)]\right\} \tag{36}$$

where A is the relaxation coefficient. f_i^{eq} is the equilibrium distribution function, expressed as

$$f_i^{eq}=E_i\phi(1+3\boldsymbol{c}_i\cdot\boldsymbol{u})+3E_i\boldsymbol{c}_i\cdot\boldsymbol{n}M_\phi\frac{4\phi(1-\phi)}{W} \tag{37}$$

where $\boldsymbol{n}$ is the normal unit vector in the gas–liquid interface region, and the interface mobility M_ϕ is related to the relaxation coefficient A as

$$M_\phi=\frac{1}{6}(1-A)\Delta x \tag{38}$$

The conserved Allen–Cahn equation, Eq. (34), can be derived from the MLKS formulation in Eq. (37) by the same procedure as used for the previous pressure equation or Navier–Stokes equation. Tayler expansion is applied to $t+\Delta t$ and $\boldsymbol{x}-\boldsymbol{c}_i\Delta x$ up to the first and the second orders, respectively, for the terms $\phi(\boldsymbol{x},t+\Delta t)$, $f_i^{eq}(\boldsymbol{x}-\boldsymbol{c}_i\Delta x,t)$ and $\phi(\boldsymbol{x}-\boldsymbol{c}_i\Delta x,t)$ in Eq. (36). The detailed derivation will be presented in the next section, where Eq. (37) for a two-phase system is expanded for a multi-phase system.

The MLKS calculation is performed in dimensionless time and space in the same manner as for LBM. Other physical phenomena, such as the temporal temperature field, melting and solidification, are calculated using dimensional formulations. Transformation between dimensionless values and dimensional values obeys the following relations:

$$\begin{cases} \boldsymbol{c}_i=\dfrac{\widehat{\boldsymbol{c}_i}}{\widehat{c}},x=\dfrac{\widehat{\boldsymbol{x}}}{\widehat{L}},u=\dfrac{\widehat{\boldsymbol{u}}}{\widehat{c}},t=\dfrac{\widehat{t}}{\widehat{t_0}},\rho=\dfrac{\widehat{\rho}}{\widehat{\rho_0}}, \\ g_i=\dfrac{\widehat{g_i}\cdot\widehat{L}}{\widehat{c}^2},p=\dfrac{\widehat{p}}{\widehat{\rho_0}\bullet\widehat{c}^2},\sigma=\dfrac{\widehat{\sigma}}{\widehat{\rho_0}\bullet\widehat{c}^2\bullet\widehat{L}},\mu=\dfrac{\widehat{\mu}}{\widehat{\rho_0}\bullet\widehat{c}\bullet\widehat{L}} \\ M_\phi=\dfrac{\widehat{M_\phi}}{\widehat{c}\bullet\widehat{L}}. \end{cases} \tag{39}$$

where the superscript $\widehat{}$ means the dimensional value. $\widehat{\rho_0}$ is the characteristic density and is defined as equal to the atmosphere gas density $\widehat{\rho_G}$ in this study. The dimensional lattice spacing $\widehat{\Delta x}$ is set to the same value as the grid length of the finite difference method for the following MPFM and thermal analysis.

2.2. Multi-Phase modified lattice kinetic scheme formulation for the conserved Allen–Cahn equation

In the LPBF process, the system consists of three phases, i.e., gas, liquid and solid, when a melt pool exists. Lee and Kim proposed a conserved Allen–Cahn equation for a multi-phase system as follows [58]:

$$\begin{aligned}\mathrm{Sh}\frac{\partial\phi_i}{\partial t}+\frac{\partial}{\partial x_\alpha}(u_\alpha\phi_i)=M_\phi\Bigg\langle&\frac{\partial}{\partial x_\alpha}\left\{1-\frac{1}{|\nabla\phi_i|}\frac{4\phi_i(1-\phi_i)}{W}\right\}\frac{\partial\phi_i}{\partial x_\alpha}\\&-\frac{\phi_i^2}{\sum_{k=1}^{N}\phi_k^2}\sum\nolimits_{j=1}^{N_p}\left[\frac{\partial}{\partial x_\alpha}\left\{1\right.\right.\\&\left.\left.-\frac{1}{|\nabla\phi_j|}\frac{4\phi_j(1-\phi_j)}{W}\right\}\frac{\partial\phi_j}{\partial x_\alpha}\right]\Bigg\rangle\end{aligned} \tag{40}$$

here, N_p is the number of phases in the system. ϕ_i is the phase order of the i phase. The following restrictions are defined:

$$\sum\nolimits_{i=1}^{N_p}\phi_i=1,\ 0\le\phi_i\le1 \tag{41}$$

The second term on the right-hand side of Eq. (40) has a feature maintains the condition of Eq. (41). In this study, N_p=3 and i = 1: Gas, 2: Liquid, 3: Solid. The solid phase order ϕ_{Solid} is varied by multi-phase field method calculations as shown in Fig. 1. Thus, the ϕ_{Solid} distribution is fixed at each time step in Eq. (39). In other words, ϕ_{Gas} and ϕ_{Liquid} are solved by Eq. (40) with the fixed ϕ_{Solid} distribution at each time step.

If Eq. (40) is directly solved by some discretized method, such as the finite difference method or finite volume method, it will consume a large amount of calculation time and lose the advantage of MLKS for flow. Therefore, the MLKS formulation of Eq. (40) must be coupled with the pressure and flow calculations in Eq. (1) and Eq. (15), respectively. It can be derived by the following procedure. During the derivation of Eq. (34) from Eq. (36), it is found that Eq. (34), except for the convection term,

$$Sh\frac{\partial\phi}{\partial t}=\frac{\partial}{\partial x_\alpha}\left\{M_\phi\left[1-\frac{1}{|\nabla\phi|}\frac{4\phi(1-\phi)}{W}\right]\frac{\partial\phi}{\partial x_\alpha}\right\} \tag{42}$$

is expressed as follows:

$$\begin{cases}\phi(\boldsymbol{x},t+\Delta t)=\sum\nolimits_{i=1}^{N_p}\left\{\xi_i^{\mathrm{eq}}(\boldsymbol{x}-\boldsymbol{c}_i\Delta t,t)+AE_i[\phi(\boldsymbol{x},t)-\phi(\boldsymbol{x}-\boldsymbol{c}_i\Delta t,t)]\right\}, \\ \xi_i^{\mathrm{eq}}=E_i\phi+3E_i\boldsymbol{c}_i\cdot\boldsymbol{n}M_\phi\dfrac{4\phi(1-\phi)}{W}.\end{cases} \tag{43}$$

The right-hand side of Eq. (42) is obtained as

$$\begin{aligned}&\frac{\partial}{\partial x_\alpha}\left\{M_\phi\left[1-\frac{1}{|\nabla\phi|}\frac{4\phi(1-\phi)}{W}\right]\frac{\partial\phi}{\partial x_\alpha}\right\}\\&=\sum\nolimits_{i=1}^{N_p}\left\{\xi_i^{eq}(\boldsymbol{x}-\boldsymbol{c}_i\Delta t,t)+AE_i[\phi(\boldsymbol{x},t)-\phi(\boldsymbol{x}-\boldsymbol{c}_i\Delta t,t)]\right\}-\phi\end{aligned} \tag{44}$$

Applying Eqs. (36) and (44) to Eq. (40) leads to the MLKS

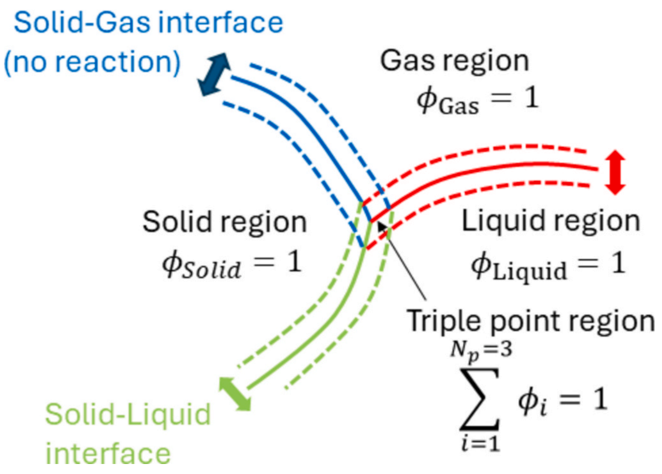

Fig. 1. Schematic illustration of the gas–liquid–solid multi-phase field.

formulation of the multi-phase CAC equation:

$$\begin{cases} \phi_i(\boldsymbol{x},t+\Delta t)=\sum_{j=1}^{N}\left\{f_j^{\mathrm{eq}}\left(\boldsymbol{x}-\mathbf{c}_j\Delta t,t\right)+AE_j\left[\phi_i(\boldsymbol{x},t)-\phi_i\left(\boldsymbol{x}-\mathbf{c}_j\Delta t,t\right)\right]\right\} \\ -\frac{\phi_i^2}{\sum_{k=1}^{N_p}\phi_k^2}\sum_{j=1}^{N_p}\left\langle\sum_{k=1}^{N}\left\{\xi_k^{\mathrm{eq}}\left(\boldsymbol{x}-\mathbf{c}_k\Delta t,t\right)+AE_k\left[\phi_j(\boldsymbol{x},t)-\phi_j\left(\boldsymbol{x}-\mathbf{c}_k\Delta t,t\right)\right]\right\}-\phi_j(\boldsymbol{x},t)\right\rangle, \\ f_j^{\mathrm{eq}}=E_j\phi_i\left(1+3\boldsymbol{c}_j\cdot\boldsymbol{u}\right)+3E_j\boldsymbol{c}_j\cdot\boldsymbol{n}M_\phi\frac{4\phi_i(1-\phi_i)}{W}, \\ \xi_k^{\mathrm{eq}}=E_k\phi_j+3E_k\boldsymbol{c}_k\cdot\boldsymbol{n}M_\phi\frac{4\phi_j\left(1-\phi_j\right)}{W}, i=Liquid,Gas,Solid. \end{cases} \tag{45}$$

Equation (45) will give precise gas and liquid order values while maintaining the condition of Eq. (41) in the triple point region.

2.3. Multi-Phase field method for melting and solidification

The following standard multi-phase field equation is introduced to simulate melting and solidification in a multi-grain system as shown in Fig. 1 [59]:

$$\frac{\partial\phi_i}{\partial\hat{t}}=\sum_{j=1}^{N_p}\frac{K_{ij}}{N}\left\{\left(\frac{\delta G}{\delta\phi_j}-\frac{\delta G}{\delta\phi_i}\right)+\frac{2\pi}{\widehat{\delta_{MPF}}}\sqrt{\phi_i\phi_j}\,\Delta g_{ij}\right\} \tag{46}$$

here, ϕ_i represents the gas, liquid or solid grain order values that are defined as $0\le\phi_i\le1$. N is the number of coexisting phase or grain at a point in the interface region. K_{ij} is the phase field interface mobility parameter. G is free energy. $\widehat{\delta_{MPF}}$ is the interface thickness. Δg_{ij} is the interface driving force that is estimated by $\Delta g_{ij}=\Delta S(T_M-T)$, where ΔS is entropy of fusion. T_{M} is the melting temperature. The deviation of free energy with order $\delta G/\phi_i$, with consideration for anisotropy in the liquid–solid interface, is expressed as

$$\frac{\delta G}{\delta\phi_i}=\sum_{j=1}^{N_p}\left\{-\frac{\partial}{\partial x_p}\left[\varepsilon_{ij}\frac{\partial\varepsilon_{ij}}{\partial\left(\nabla_p\phi_j\right)}\left(\nabla\phi_j\right)^2\right]+\varepsilon_{ij}\nabla\varepsilon_{ij}\cdot\nabla\phi_j+\frac{1}{2}\varepsilon_{ij}^2\nabla\right.$$
$$\left.\bullet\nabla\phi_j+W_{ij}\phi_j\right\} \tag{47}$$

where ε_{ij} and W_{ij} are phase field parameters related to the interface energy $\widehat{\sigma_{ij}}$ and interface thickness δ_{MPF}. Anisotropy of 3D four hold symmetry for the solid–liquid interface is defined to be a trigonometrical function ε_{ij} as follows [65]:

$$\varepsilon_{ij}=\overline{\varepsilon_{ij}}\zeta_{ij},\ \ \zeta_{ik}=1-\widetilde{\varepsilon}\left\{3-4\left(n_1'^4+n_2'^4+n_3'^4\right)\right\}$$

where $\overline{\varepsilon_{ij}}$ is the is isotropic constant, ζ_{ij} is the normalized trigonometrical function and $\widetilde{\varepsilon}$ is its amplitude. n'_i is the relative unit vector to the preferential growth orientation of solid crystal, which is explained as follows:

$$\begin{cases} \boldsymbol{n}'_i=a_{ij}\bullet\boldsymbol{n}_j, \\ a_{ij}=\begin{bmatrix}\cos\varphi\cos\theta & \cos\varphi\sin\theta & \sin\varphi \\ -\sin\theta & \cos\theta & 0 \\ -\sin\varphi\cos\theta & -\sin\varphi\sin\theta & \cos\varphi\end{bmatrix}, \end{cases} \tag{49}$$

where n_j is the unit normal vector in the liquid–solid interface region, and a_{ij} is the directional cosine of the crystalline unit vector of grain. θ and φ are the Euler angle relative to the x-coordinate on the x-y plane and the angle relative to the x-y plane, respectively, in Cartesian coordinates x-y-z. It is provided for the MPFM parameters, $\overline{\varepsilon_{ij}}$ and W_{ij}, to be related to the reference interfacial energy $\overline{\sigma}_{ij}$ and the interface thickness $\widehat{\delta_{\mathrm{MPF}}}$ as follows [59]:

$$\overline{\varepsilon}_{ij}^2=\frac{8}{\pi^2}\overline{\sigma}_{ij}\widehat{\delta_{MPF}},\ W_{ij}=\frac{4\overline{\sigma}_{ij}}{\widehat{\delta_{MPF}}} \tag{50}$$

By using these relations, the phase field mobility K_{ij} in Eq. (46) is defined to be related with M_{ij} as follows:

$$K_{ij}=\frac{\pi^2}{4\widehat{\delta_{\mathrm{MPF}}}}M_{ij} \tag{51}$$

Substituting Eqs. (47)–(49) into Eq. (46) leads to an executable formulation in the computation program. The MPFM equation, Eq. (17), is solved by the finite difference method using a constant grid width equal to the dimensional lattice spacing of MLKS. The MPFM equation is assumed to be effective only for the solid–liquid interface region. The gas–liquid and gas–solid interfaces are set to be nonreactive, with their phase field mobilities defined as zero.

2.4. Thermal analysis

The following temperature diffusion equation with a convective term, which is effective in the gas or liquid flow fields, is applied to thermal analysis in this study:

$$\frac{\partial T}{\partial\hat{t}}+\nabla\bullet(T\boldsymbol{u})=k\nabla^2T+Q_{bm}+Q_{lt}+Q_{evap}+Q_{rad} \tag{52}$$

here, T is temperature and k is the temperature diffusion coefficient defined by

$$k=k_{Gas}\phi_{Gas}+k_{Liquid}\phi_{Liquid}+k_{Solid}\phi_{Solid} \tag{53}$$

where k_{Gas}, k_{Liquid} and k_{Solid} are the temperature diffusion coefficients of the gas, liquid and solid phases given as

$$k_{Gas}=\frac{\lambda_{Gas}}{\rho_{Gas}\bullet c_{p_{Gas}}},k_{Liquid}=\frac{\lambda_{Liquid}}{\rho_{Liquid}\bullet c_{p_{Liquid}}},k_{Solid}=\frac{\lambda_{Solid}}{\rho_{Solid}\bullet c_{p_{Solid}}} \tag{54}$$

where λ_{Gas}, λ_{Liquid} and λ_{Solid} are the thermal conductivities of the gas, liquid, and solid phases, respectively. $c_{p_{Gas}}$, $c_{p_{Liquid}}$ and $c_{p_{Solid}}$ are the specific amounts of heat in the gas, liquid, and solid phases, respectively. Q_{bm}, Q_{lt}, Q_{evap} and Q_{rad} in Eq. (52) are the volumetric heat of the laser beam absorption $\widehat{Q}_{bm}$, the melting/solidification latent heat $\widehat{Q}_{\mathrm{lt}}$, the evaporation latent heat $\widehat{Q}_{\mathrm{evap}}$ and the volumetric heat radiation $\widehat{Q}_{rad}$, respectively, divided by $c_p\bullet\rho$, where $c_p\equiv c_{p_{Gas}}\phi_{Gas}+c_{p_{Liquid}}\phi_{Liquid}+c_{p_{Solid}}\phi_{Solid}$ and $\rho\equiv\rho_{Gas}\phi_{Gas}+\rho_{Liquid}\phi_{Liquid}+\rho_{Solid}\phi_{Solid}$. Equation (52) is numerically solved by the finite difference method by using a constant grid in the same manner for the constant grid in MPFM or the dimensional lattice spacing of MLKS.

The laser beam power density I_0 is assumed to obey a radius Gaussian distribution as follows:

$$\begin{cases} I_0 = \lambda_{\text{abs}}\dfrac{P}{2\pi\sigma_r{}^2}\exp\left(-\dfrac{\boldsymbol{r}^2}{2\sigma_r{}^2}\right), \\ \boldsymbol{r} = x - vt, \end{cases} \tag{55}$$

where P is laser power, $\boldsymbol{r}$ is the radius from the beam center axis, σ_r is the $1/e$ ratio radius and λ_{abs} is the absorption coefficient. This heat source is traveling with the laser beam velocity, $\boldsymbol{v} = (v_x, 0, 0)$. In this study, the beam axial direction is defined for the z-coordinate. The laser power absorption is assumed to follow the Beer–Lambert law, in which the absorbed rate for depth in the z direction is assumed to be

$$\frac{dI}{dz} = -\frac{I}{\mu_{abs}} \tag{56}$$

Integrating Eq. (56) gives

$$I = I_o Exp\left(-\frac{\Delta z_{\text{dpth}}}{\mu_{\text{abs}}}\right) \tag{57}$$

where μ_{abs} is a parameter of absorption depth. The volumetric heat of the laser beam absorption $\widehat{Q}_{\text{bm}}$ at coordinate z is expressed as

$$\widehat{Q}_{\text{bm}} = I/\Delta z \tag{58}$$

The absorption depth Δz_{dpth} for the inversed z-direction from the top surface on a liquid or solid is measured in only the liquid or solid regions, and not in the gas region. The melting/solidification latent heat $\widehat{Q}_{lt}$ is provided as

$$\widehat{Q}_{lt} = \rho_{Solid} L \cdot \dot{\phi}_{Solid} \tag{59}$$

where L is the melting/solidification latent heat and $\dot{\phi}_{\text{Solid}}$ is the time differentiation of the solid phase order of MPFM. The finding that the signs of $\widehat{Q}_{lt}$ ($\dot{\phi}_{Solid}$) for melting and solidification are negative and positive, respectively, is commensurate with these physical states. The model for heat flux caused by metal liquid evaporation heat loss proposed by Knight, which is similar to Eq. (23), is adapted in this study as follows [66]:

$$\boldsymbol{q}_{evap} = \boldsymbol{n}\beta_R L_v \sqrt{\frac{M_{SLD}}{2\pi RT}}\widehat{p}_0 \cdot exp\left[\frac{L_v M_{SLD}}{RT_{vap}}\left(1 - \frac{T_{vap}}{T}\right)\right], T \geq T_{vap} \tag{60}$$

where $\boldsymbol{n}$ is the normal unit vector on the gas–liquid interface, β_{R} is the vaporization ratio, M_{SLD} is the molar mass of metal alloy, R is a gas constant, $\widehat{p}_0$ is vapor pressure, L_{v} is the latent heat of vaporization and T_{vap} is the vaporization temperature. The heat flux $\boldsymbol{q}_{\text{evap}}$, Eq. (60), is transformed to the volumetric heat $\widehat{Q}_{\text{evap}}$ in the gas–liquid interface region by applying a continuous surface model analogous to that in Eq. (19) as follows [62]:

$$\widehat{Q}_{evap} = -\left|\boldsymbol{q}_{evap}\right| \frac{|\nabla\rho(\boldsymbol{x}, t)|}{\rho_L - \rho_G} \cdot \frac{\rho(\boldsymbol{x}, t)}{(\rho_L + \rho_G)/2} \tag{61}$$

where the minus sign shows the endothermic reaction of evaporation. The radiation heat flux $\boldsymbol{q}_{\text{rad}}$ from the gas–solid or gas–liquid surface to the gas space is expressed as

$$\boldsymbol{q}_{rad} = \boldsymbol{n}\varepsilon\sigma_{Bolz}\left(T^4 - T_0^4\right) \tag{62}$$

where σ_{Bolz} is the Stefan–Boltzmann constant, ε is the emissivity and T_0 is the atmosphere temperature. As in Eq. (61), $\boldsymbol{q}_{\text{rad}}$ can be written as the volumetric heat $\widehat{Q}_{rad}$ as follows:

$$\widehat{Q}_{rad} = -|\boldsymbol{q}_{rad}| \frac{|\nabla\rho(\boldsymbol{x}, t)|}{\rho_{S,L} - \rho_G} \cdot \frac{\rho(\boldsymbol{x}, t)}{(\rho_{S,L} + \rho_G)/2} \tag{63}$$

here, $\rho_{\text{S,L}}$ represents the solid and liquid densities, and the relation $\rho_{\text{S}} = \rho_{\text{L}}$ is assumed in this study.

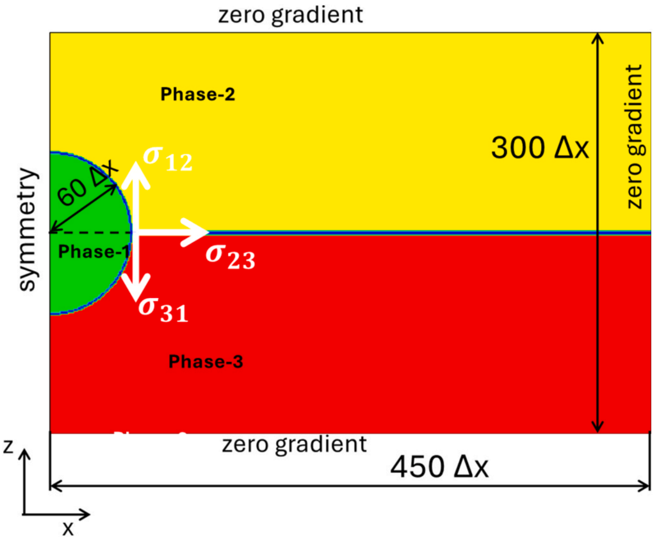

Fig. 2. Initial droplet contacting with two liquid domains.

2.5. Parallelization computing

As described above, the MLKS, the MPFM and the thermal equations are suitable for a super-computing algorithm. These are solved using MPI/OpenMP hybrid parallelized programing with the HPE SGI 8600 system at the Numerical Materials Simulator Station of the National Institute for Materials Science [67]. Intel OneAPI FORTRAN is selected for the MPI/OpenMP hybrid programing [68]. The LPBF process for the simulation is modeled as a cubic region, in which the metal-alloy base plate is set on the x-y plane at the origin of the z direction. Metal alloy powder particles are layered on the top of the base plate. Another space that does not include the solid phase is defined to be filled with the gas phase. The LPBF model region is divided for the x and y directions by the block regions of a cube, for which the grid point numbers in the x and y directions are set to be constants, respectively. MPI parallelization is performed on the small cubic regions. OpenMP is applied to "DO LOOP" of the program for the x, y and z loops in each block.

3. Validation of numerical method

The MLKS formulation of the multi-phase CAC equation represented by Eq. (45) is the novelty of this numerical method. Eq. (45) is validated in two fundamental problems consisting of three fluid phases, the equilibrium shape of the droplet in contact with two liquid domains and the bubble rising in two liquid phases as follows.

3.1. Equilibrium shape of droplet contacting with two liquid domains

The initial shapes of the droplet and two liquid phases and their dimensions are defined in Fig. 2. The cross-sectional shape for the y-direction is the same. Consequently, the two-dimensional simulation was carried out by the three-dimensional model calculation. The center of one droplet, defined as liquid-1 was placed at the center of the vertical direction on the left side of the region. A symmetrical boundary condition was applied to the left side. The boundary between the phases, liquid-2 and liquid-3, was placed horizontally at the center of the vertical direction. The triple point between three liquid phases exists at the

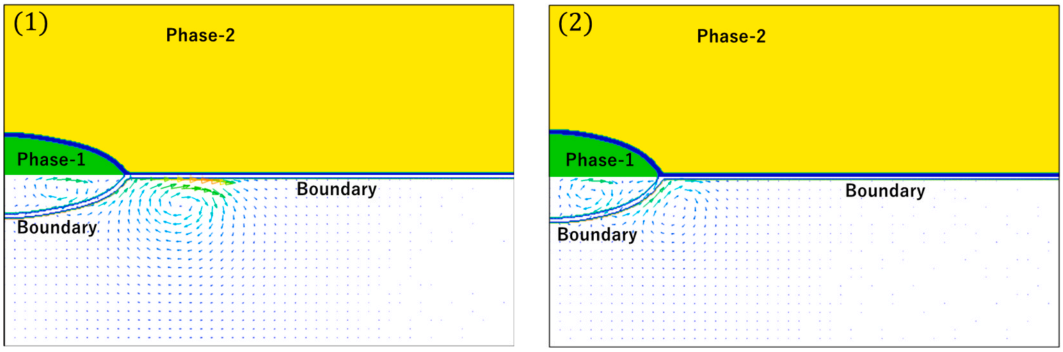

Fig. 3. Equilibrium shape of droplet contacting with two liquid domains at 45,000 time step, (1) Case-1: $\sigma_{23} = 1.732 \times 10^{-2}\mathrm{N/m}$, (2) Case-2: $\sigma_{23} = 1.0 \times 10^{-2}\mathrm{N/m}$.

right end of the droplet (liquid-1). Densities of droplet (liquid-1), liquid-2 and −3 were set to the same value, $1 \times 10^3\mathrm{Kg/m^3}$. Viscosity of droplet (liquid-1), liquid-2 and −3 were set to the same value, $1 \times 10^{-2}\mathrm{Ps{\cdot}s}$. Grid width Δx for x, y and z directions was set to 1/6400 m (0.15625 μm). Gird numbers for x, y and z directions were defined as 450, 10 and 300. The number for the y-direction was very small because the same phases and flow values were distributed in the two-dimensional space, the x-z plane. The value of surface tension between droplet and liquid-2, σ_{12}, and between droplet and liquid-3, σ_{31}, was defined as the same value, $1 \times 10^{-2}N/m$. Meanwhile, the interfacial tension between liquid-2 and −3, σ_{23}, was set to two values, $1.732 \times 10^{-2}N/m$ (Case-1) and $1.0 \times 10^{-2}N/m$ (Case-2) in order to compare equilibrium morphologies due to σ_{23} differences. The interfacial width W and the relaxation factor A of the CAC parameter were chosen as $4\Delta x$ and 0.6, respectively. The characteristic length L and the particle velocity c of the MLKS parameter were set to Δx and $50m/s$, respectively.

The volume force vector $\boldsymbol{F}_{SV}$ in the interfacial region for the interfacial tension σ is defined by Eq. (19) according to the continuous surface model [62]. In this equation, the interfacial unit normal vector $\boldsymbol{n}$ was defined by based on the density variation. However, in this test model, the density was constant in all phases. Therefore, the interface unit normal vector, Eq. (20), is defined by the gradient of the phase order ϕ_i instead of the density. $\mathbf{F}_{\mathrm{SV}}$ is expressed by considering the triple point region, as follows,

$$\begin{cases} \mathbf{F}_{\mathrm{SV}} = \frac{1}{2}\sum_{i=1}^{2}\sum_{j=2}^{3}\left[\sigma_{ij}\left(\chi_i\boldsymbol{n}_i + \chi_j\boldsymbol{n}_j\right) \bullet \xi\right], \\ \xi = B\phi_i\phi_j|\nabla\phi_i||\nabla\phi_j|, \quad B = \dfrac{15\mathrm{W}}{2\tan^{-1}(1-2\lambda)}, \quad \lambda := 0.1 \end{cases} \tag{64}$$

where the integration of ξ for the normal direction in the interface becomes unit [69].

The equilibrium morphologies of Cases −1 and −2 achieved at 45,000 time step of MLKS. The phase and flow velocity vector distributions with interface lines of Case −1 and −2 are shown in Fig. 3. The density and viscosity of all liquid phases are the same values, respectively. Therefore, the phase and flow velocity vector distributions are symmetric for the horizontal line at the center for the vertical direction. Half of the upper and lower distributions show phase and velocity vector distributions, respectively, in Fig. 3. The flow is driven by interfacial tension with curvature as expressed in Eq. (19). The phase interface is transformed by the flow velocity according to the phase order convection term of Eq. (40). It is expected that the larger tension σ_{23} of Case-1 will result in a larger velocity around the interface between liquids −2 and −3 than Case-2. The higher velocity of Case-1 shifts the triple point more to the right than Case-2. In fact, it is confirmed that the maximum velocity around the interface between liquids −2 and −3 is greater in Case-1 than in Case-2 and the horizontal length of the droplet (liquid-1) is longer in Case-1 than in Case-2. According to the equilibrium between the interfacial tensions at the triple point, the angle of the droplet becomes 60 deg. and 120 deg. in Cases −1 and −2 respectively. The one of Case-2 is nearly 120 deg. Meanwhile, the one of Case-1 is around 90 deg. It is considered reasonable by reasoning as follows. The flow boundary layer occurs around and inside in the interface region between liquid −1 and −2, as can be seen in the flow velocity vector distribution of Fig. 3. This finite flow boundary layer thickness is considered to increase the angle of the droplet side at the triple point compared to that determined by the equilibrium between the interfacial tensions. This slight difference is not an issue in this study. The triple point dose not move at each time step because the third phase is defined as a solid that does not flow. The MLKS equation of the multi-phase CAC, Eq. (45), has the property of keeping the summation of the phase orders of gas, liquid and solid as one in this study.

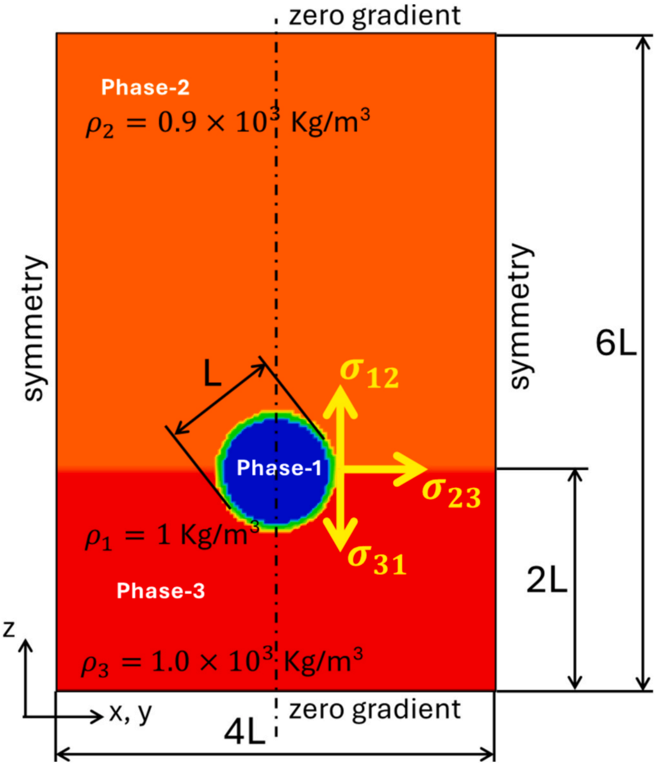

Fig. 4. Dimensions for initial bubble in two liquid phases.

3.2. Bubble rising in two liquid phases

The purpose of this study is to understand gas pore dynamics in LPBF simulation. The accurate prediction of gas bubble motion behavior in two liquid phases needs to be confirmed in this test calculation. Some

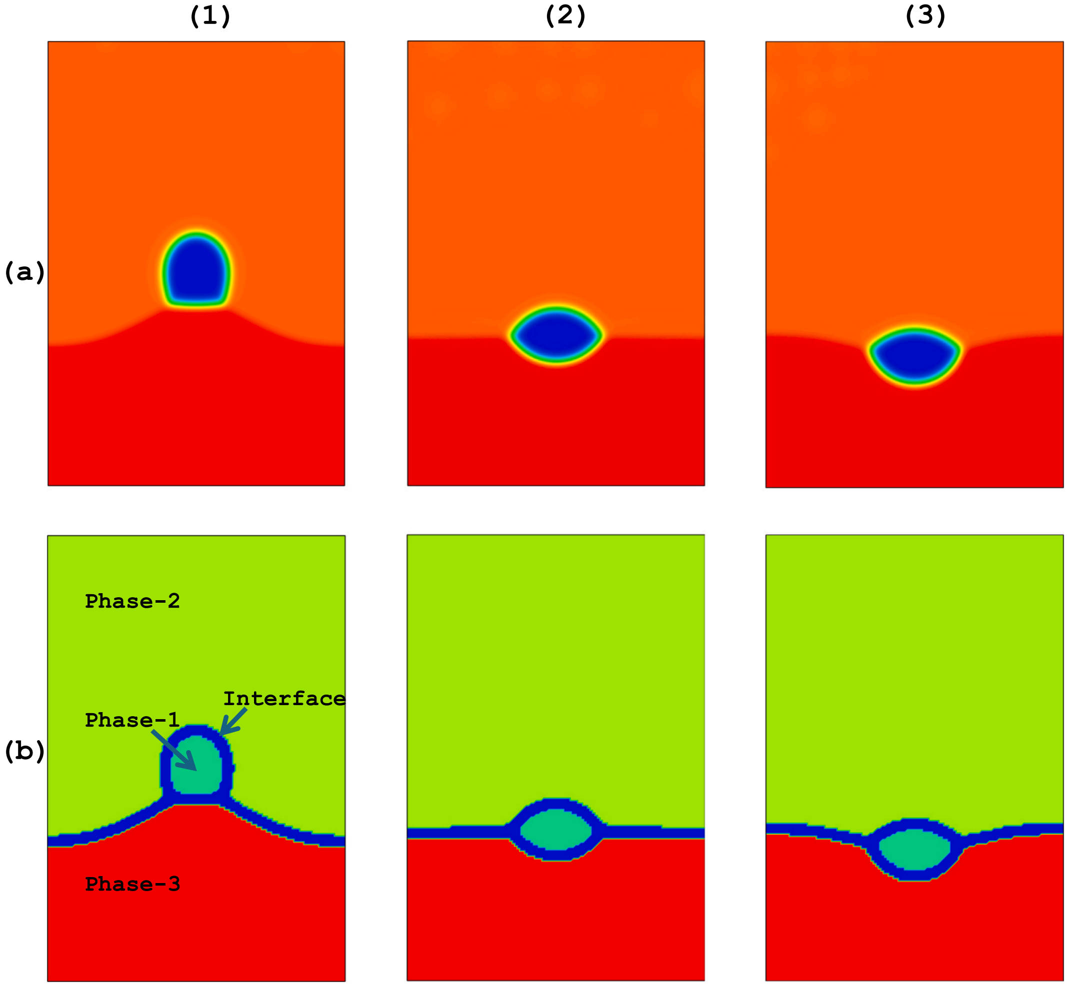

Fig. 5. Equilibrium bubble morphologies in two liquid phases with interface, (a) density and (b) phase distributions, for (1) Case-1, (2) Case-2 and (3) Case-3.

verification model calculations have been performed by Boyer *et. al.* [70] and Aihara *et. al.* [71]. Boyer *et. al.* proposed the Cahn-Hilliard equation adapted to follow the phase boundary motion instead of the Allen-Cahn equation. Aihara *et. al.* presented finite difference approach to solve phase interface tracking coupled with Navier-Stokes equation. The initial shapes of bubble and two liquid phases and their dimensions were defined in Fig. 4. It shows the center cross section for x and y directions. The diameter of the spherical bubble was set as $L = 30\Delta x$. Δx is the grid width, which is constant for x, y and z directions. Phase-2 and phase-3 (liquid phases) were distributed for vertical direction by upper length $4L$ and lower length $2L$, respectively. The center of the bubble was placed at the centers for x and y directions at the interface between phases −1 and −2. The grid width Δx was set to 1/6400 m (0.15625 μm). The densities of the bubble (gas phase), phases −2 and −3 were chosen as $1Kg/m^3$, $0.9 \times 10^3 Kg/m^3$ and $1 \times 10^3 Kg/m^3$, respectively. The difference in densities between bubble and phase-3 is close to the practical ratio of gas to liquid. Slightly lower density of phase-2 than phase-3 makes no natural convection between phases −2 and −3. Bubble has buoyancy force due to gravity. However, the bubble floating motion must be influenced by interfacial tensions. The viscosity of the bubble (gas phase), phases −2 and −3 were set to $1.83 \times 10^{-5} Ps{\cdot}s$, $1.0 \times 10^{-3} Ps{\cdot}s$, and $1.0 \times 10^{-5} Ps{\cdot}s$, respectively. These values are also close to the practical ones of gas and liquid. The surface tension values between bubble and phase-3, σ_{31}, and between phases −2 and −3, σ_{23}, were defined as the same value, 1N/m. Meanwhile, the interfacial tension between the bubble and phase-2, σ_{12}, was set at three values, $0.3N/m$ (Case-1), $1.0N/m$ (Case-2) and $1.5N/m$ (Case-3) in order to compare the equilibrium bubble morphologies due to σ_{12} differences. The interfacial width W and the relaxation factor A of the CAC parameter were chosen as $4\Delta x$ and 0.6, respectively. The characteristic length L and the particle velocity c of the MLKS parameter were set to Δx and $20\ 0m/s$, respectively.

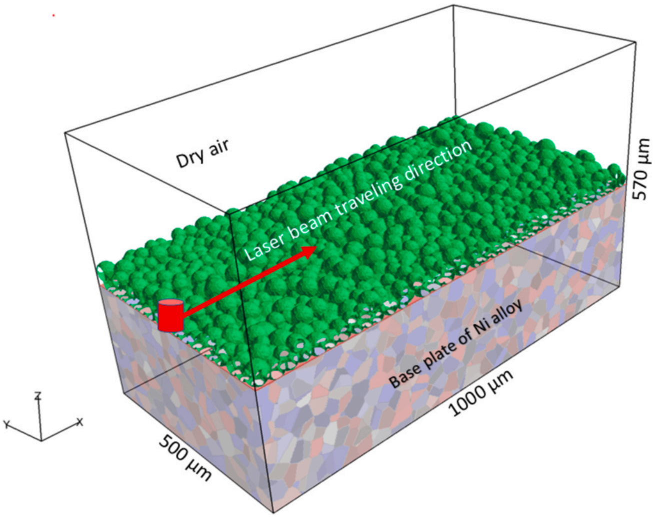

Fig. 6. LPBF model dimension and alloy powder distribution.

The density and phase distributions with interface of each case are shown in Fig. 5. The blue region shows the interface region between the phases. Its width is confirmed to be maintained by four grids as entered in the CAC equation. In Case-1, the bubble morphology reached the equilibrium shape. The critical radius of the bubble, r_c, to detach from the interface of phases -3 and 2 can be promptly obtained by the balance between the buoyancy of the bubble and the pulling force integrated by σ_{23} on the circumference of the bubble sphere as follows,

$$r_c = \sqrt{\frac{3}{2}\frac{\sigma_{23}}{(\rho_2 - \rho_1)g}} \tag{65}$$

Substituting σ_{23}, ρ_2 and ρ_1 into Eq. (65) gives $r_c = 1.24 \times 10^{-2}$ m. Consequently, it is confirmed that bubble does not detach from the phase-3 boundary and reach equilibrium morphology because the radius of the initial bubble sphere, 2.34×10^{-3} m, is smaller than r_c. Case-1 reached the equilibrium condition after 30,000 non-dimensional time steps. Other Cases -2 and -3 also reach their own equilibrium shapes at the same time steps of 20000. Each equilibrium shape and position for the z-direction is determined by the balance between the interfacial tensions, σ_{12}, σ_{23}, σ_{31}, and the buoyancy of the bubble. In Case-1, the bubble is placed above the initially vertical position of the interface between phases -1 and -2 and is stretched in the vertical direction to compensate for the small value of σ_{12}. Meanwhile, in Case-3, it can be seen that larger σ_{12} sinks the equilibrium z-position from the initial phases -2 and -3 interface than other cases. In Case-2, the equilibrium z-position is almost neutral and rises slightly because all the interface tensions are equal, and the buoyancy of the bubble is relatively smaller than the interfacial tensions due to the large difference between r_c and the bobble radius. In Cases -2 and -3, the widths of the equilibrium bubble shapes are longer than in Case-1 because of the dominant control of the interfacial tensions. These tendencies are confirmed in agreement with the results of Aihara *et. al.* [71].

4. Physical and numerical conditions

4.1. LPBF model and process parameters

The LPBF model in this study is illustrated in Fig. 6**.** The model size was set as 1000μm, 500μm and 570μm for the x, y and z directions, respectively. The laser beam is defined as traveling in the x direction. The grid width $\Delta\widehat{x}$ of the finite difference method for MPFM and the thermal equations, Eqs. (46) and (52), was set at 2×10^{-6}m. The characteristic length $\widehat{L}$ was defined as 2×10^{-3}m. The nondimensional grid width, $\Delta x := \Delta\widehat{x}/\widehat{L}$, became 1×10^{-3}, which was adapted to the flow and CAC MLKS equations. The numbers of grids in the region were $500 \times 250 \times 285$. The Ni alloy base plate thickness was 260 μm. The base plate was defined to consist of equiaxed grains generated by a Voronoi diagram, the average diameter of which was 30 μm. The number of base plate grains by this definition was 9196. These grains were provided their own crystalline angles as preferential growth orientation angles, θ and φ of Eq. (49), which were randomly generated. In Fig. 6, the colors of the base plate grains show Euler angle φ differences. The particles of the Ni alloy powder were assumed to be spherical in shape. The average radius and its standard deviation of the powder were defined as 30 μm and 6 μm, respectively. The particle distribution was generated by using the discrete element method (DEM) under the condition of a powder layer thickness of 30 μm with 1000 particles [72]. These powder particle dimensions are practical values for the experimental conditions for Ni alloy in our laboratory. The powder particles were also provided with their own preferential growth orientation angles, θ and φ. The space above the powder layer and between the power particles was assumed to be filled with dry air atmosphere. The characteristic particle velocity $\widehat{c}$ for nondimensionalization of MLKS was set as 20 m/s. The Strouhal number, Sh, was defined as the unit in this study. These parameter and characteristic values are equivalent to the characteristic time $\widehat{t_0} = \widehat{L}/\widehat{c}/Sh$, 1×10^{-4}s and the characteristic velocity $\widehat{U} = \widehat{c}$. The time difference for MPFM, $\Delta\widehat{t}_{\mathrm{MPFM}}$, was set at 1×10^{-6}s. The dimensional time step of MLKS became $\Delta\widehat{t} = \Delta\widehat{x}/\widehat{c} = 1 \times 10^{-7}$s. Therefore, MLKS calculations were performed ten times per one MPFM finite difference calculation. The same treatment was adapted for the thermal equation.

Table 2
Laser beam conditions, Eqs. (55) and (56).

Parameter	Symbol	Value
Beam radius (1/e ratio radius)	σ_r	40 μm
Traveling velocity	$\boldsymbol{v}$	1 m/s
Beam power	P	400 W
Absorption depth	μ_{abs}	70 μm
Absorption coefficient	λ_{abs}	0.7

Table 3
Physical properties.

Property	Symbol	Value	Eq. No.	Reference
Density of liquid	ρ_{L}	7118 Kg/m^3	4	[75]
Viscosity of liquid	μ_{L}	7×10^{-3} Pa·s	17	[76]
Surface tension gas/liquid	σ_{GL}	1.8 J/m^2	19	[77]
Marangoni coefficient	ξ_{Mar}	-1×10^{-4} J/m^2/K	22	[75]
Melting temperature	T_{M}	1574 K	22, 24	[75]
Vaporization ratio	β_{R}	0.5	23, 60	
Boiling temperature	T_{vap}	3335 K	23, 60	[74]
Vapor pressure	$\widehat{p}_0$	1 atm	23, 60	
Latent heat of vaporization	L_{v}	6.69×10^{6} J/Kg	23, 60	[75]
Molar mass of solid	M_{SLD}	5.87×10^{-2} Kg/mol	23, 60	[75]
Thermal expansion coefficient of gas	β_{G}	6.25×10^{-4} 1/K	24	
Thermal expansion coefficient of liquid	β_{L}	1.29×10^{-4} 1/K	24	[74]
Interface energy solid/liquid	σ_{SL}	0.5 J/m^2	50	[19]
Thermal conductivity of gas	λ_{Gas}	0.024 W/m/K	54	[75]
Thermal conductivity of liquid	$\lambda_{\mathrm{Liquid}}$	6.7 + 0.014 • TW/m/K	54	[75]
Thermal conductivity of solid	λ_{Solid}	6.7 + 0.0136 • T W/m/K	54	[75]
Heat capacity of gas	cp_{Gas}	1000 J/Kg/K	54	[75]
Heat capacity of liquid	cp_{Liquid}	754 J/Kg/K	54	[75]
Heat capacity of solid	cp_{Solid}	643 J/Kg/K	54	[75]
Latent heat of fusion	L	2.66×10^{5} J/Kg	59	[75]
Atmosphere temperature	T_0	293 K	62	
Emissivity	ε	0.7	62	[75]

Table 4
Numerical parameters.

Parameter	Symbol	Value	Eq. No.
Relaxation parameter for CAC	A	4 (non-dimension)	38, 45
Interface width for CAC	W	5	37, 45
Interface mobility for MPFM	K_{LS}	1×10^{-8} m^4/J/s [19]	46, 51
Interface width for MPFM	$\widehat{\delta_{\mathrm{MPF}}}$	5 Grid [19]	46, 50
Anisotropy amplitude	$\widetilde{\varepsilon}$	1/30 [19]	48

The previous time step, $\Delta\widehat{t}$, was confirmed to be a stable condition according to the stability criterion of capillarity and viscosity in view of the CFD method as follows, respectively [73]:

$$\Delta\widehat{t}_{\sigma} = \sqrt{\frac{(\rho_{\mathrm{L}} + \rho_{\mathrm{G}}) \bullet (\Delta\widehat{x})^{3}}{4\pi\sigma_{\mathrm{GL}}}} \tag{66}$$

and

$$\Delta\widehat{t}_{\mu} = \frac{\rho_{\mathrm{L}}(\Delta\widehat{x})^{2}}{6\mu_{\mathrm{L}}} \tag{67}$$

By using the following physical constants, $\Delta\widehat{t}_{\sigma}$ and $\Delta\widehat{t}_{\mu}$ were

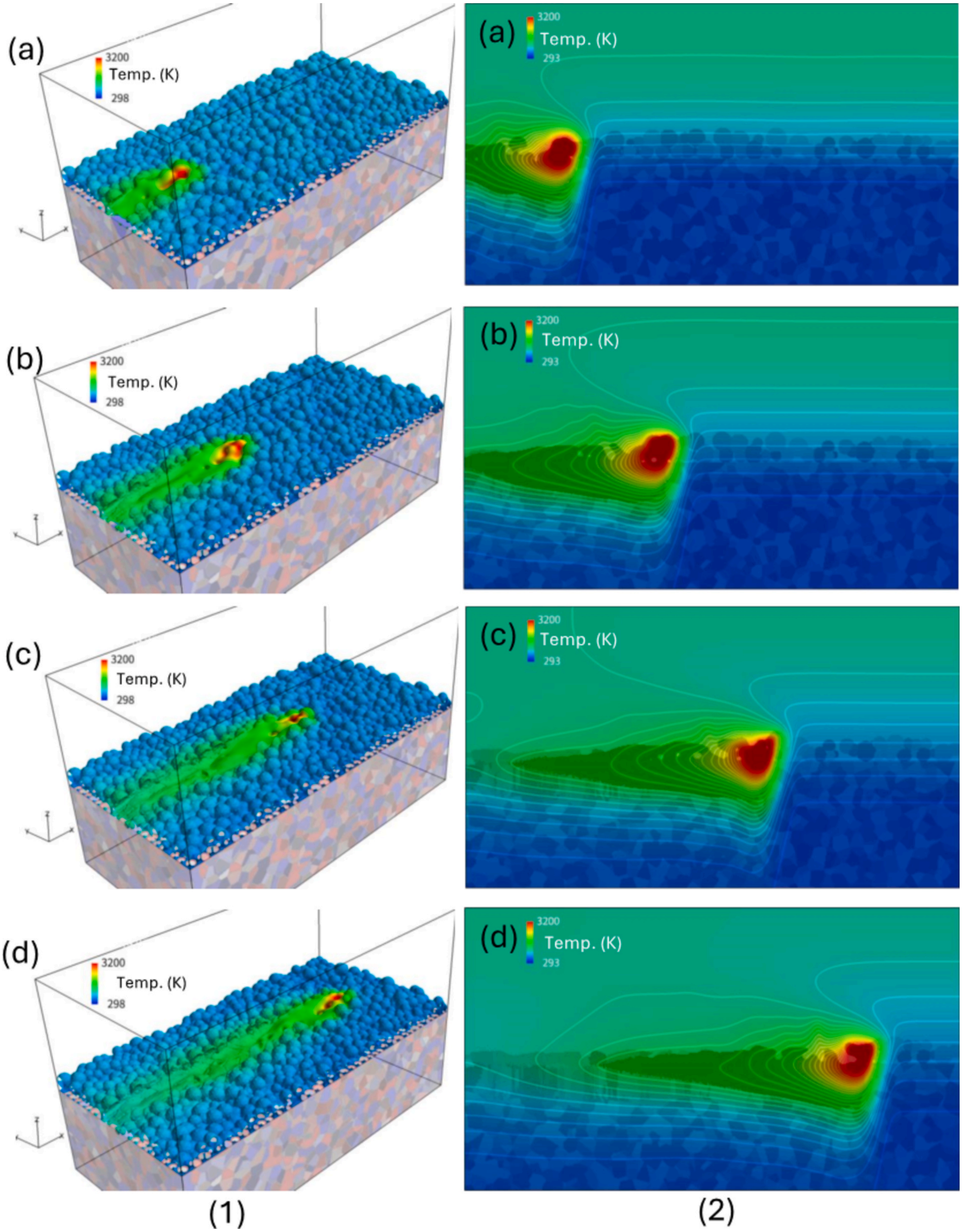

Fig. 7. (1) Temporal melt pool surfaces and powder particles with the temperature distributions. (2) Temperature and grain distributions on a cross-section in the center of the width (y) directions (a) 0.2 ms, (b) 0.4 ms, (c) 0.6 ms, (d) 0.8 ms.

estimated as 1×10^{-7}s and 7.0×10^{-7}s, respectively.

Simulation for the single track of the laser beam traveling for the x-direction was performed as shown in Fig. 6. The beam was set to start from the root of the x-direction at the center of the y-direction. The beam traveling velocity and the power P in Eq. (55) were 1 m/s and 400 W, respectively, which were practical values for the experimental conditions. The laser beam condition values in Eqs. (55) and (56) are summarized in Table 2. The absorption depth, μ_{abs}, and the absorption coefficient, λ_{abs}, were decided after some trial calculations.

The physical constants according to the equations in the previous section are listed in Table 3. In this study, calculations were performed by using the physical constants of an Ni alloy, IN738LC. The density ratio of gas by liquid, ρ_G/ρ_L, was assumed to be 500. This value was considered large enough for approximation of the gas atmosphere. The viscosity ratio of gas by liquid, μ_G/μ_L, was assumed to be 382.5. This resulted in an actual air value of 1.83×10^{-5}Pa • s in 273 K. The melting temperature T_M was defined as the average value of the equilibrium liquidus and solidus temperatures, 1489 K and 1614 K, respectively, obtained by Thermo-Calc Software [74]. In Eqs. (23) and (60), the vaporization ratio β_R and $\widehat{p}_0$ were assumed to be 0.5 and 1 atm, respectively, as control parameters. The thermal expansion coefficient of gas, β_G, was approximated by the ideal gas formulation, 1/T, under the assumption of a gas temperature of 1600 K around the melt pool. The thermal expansion coefficient of liquid, β_L, was obtained by using Thermo-Calc Software [74] under condition of a molar volume difference from 1600 K to 2000 K for Inconel738LC composition. The atmosphere temperature for radiation, T_0, and the initial base plate temperature were defined as room temperature: 293 K. However, the initial gas region temperature in Fig. 6 was assumed to be 1273 K due to the restriction on large cooling in the early stage.

Numerical parameter values for the MLKS formulation of the multiphase CAC equation, Eq. (45), and MPFM equation, Eq. (46), are listed in Table 4. The relaxation parameter A and interface width W for CAC were decided after some trial calculations to obtain a stable result.

The boundary condition of temperature on the outer surface in Fig. 6 was set as insulation under a gradient condition. Therefore, the outflow of heat from the system was promoted by the radiation expressed by Eq. (62). The zero gradient and symmetry conditions were applied to the pressure and velocity conditions of gas and liquid flows, respectively. The boundary condition for the order variable of MPFM was also set as the zero-gradient condition.

The MPI parallelization was set to 25 by dividing the LPBF model region, Fig. 6., into five blocks for the x and y directions. The number of grids in each block for the x and y directions were set to 100 and 50, respectively. The boundary grid point data between these blocks were transformed by using the MPI data passing function at each time step. Open-MP parallelization is also performed for "DO LOOP" of the program in each program to accelerate the overall computation speed. The number of cores for MPI parallelization was set to 300 in the present calculation.

5. Results and discussion

The calculation was performed in 1200 time steps, of which the travelling length was 1200 μm. The last 200 steps were used for the solidification progress in the melt pool around the LPBF model for the beam travelling direction. The calculation time was measured to be 2.45 min per time step. The calculation time for a beam travel length of 1000 μm (length of the LBPF model for the x-direction) was approximately 41 h. This was considerably less than the 60 h required by our LPBF CFD calculation [78]. This method includes not only flow field and solid/liquid transformation calculations, but also solidification microstructure transformation in a single calculation run.

Fig. 7 shows the temporal melt pool surfaces and powder particles with the temperature distributions (column (1)), and temperature and grain distributions on cross-section in the center of the width (y-direction) (column (2)). The base plate grain distributions are also shown in Fig. 7. The color variation for the base plate grain shows the differences in the crystalline Euler angle φ. It can be seen that powder particles and base plate grains promptly melt with beam traveling, where the temperature rapidly increases over melting temperature. At the same time, the melt pool surface in the high temperature region is depressed by the recoil pressure of metal absorption. The depressed surface does not retain a keyhole shape. It intermittently repeats an up and down movement, as shown in the panels in column (2) of Fig. 37 This is because the Beer–Lambert model, Eq. (57), of beam absorption does not

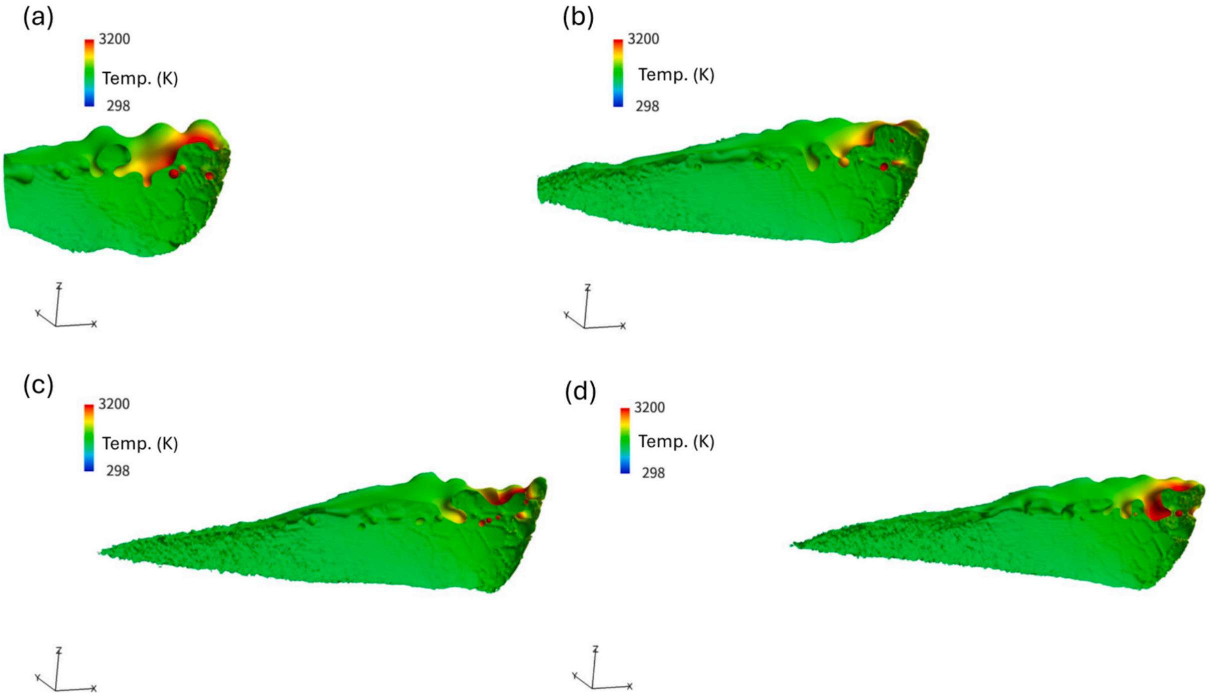

Fig. 8. Temporal melt pool surfaces and powder particles with the temperature distributions (a) 0.2 ms, (b) 0.4 ms, (c) 0.6 ms, and (d) 0.8 ms.

provide a digging effect like a ray tracing model.

On the other hand, it can also be seen that gas pores are generated from the initial space between the powder particles in the melt pool. These gas pores are transported by liquid flow convection and buoyancy and finally go out into the atmosphere. The transportation of gas pores also seems to collide with the hole generated by the recoil pressure in column (2) of Fig. 7. This interaction also accelerates the complex melt pool flow and surface movement. The pores expelled from the melt pool can be seen as a hole around the rear of the beam absorbed area in Fig. 7 (column (1)). As the pores disappear, the vertical position of the melt pool surface gradually drops.

In Fig. 7 (column (2)), the melt pool depth becomes maximum just after melting and gradually decreases with the progress of solidification by cooling. The melt pool length for the beam traveling direction seems to be relatively longer than Rosenthal's analytical solution [79], in which melting latent heat is not considered. In the present method, the latent heat included in the thermal equation, Eq. (52), has a reheating effect that reduces the local cooling rate. Furthermore, the flow convection in the melt pool promotes the uniformity of temperature. Then, it lengthens the melt pool.

In order to see the gas pore generation and transportation more clearly, Fig. 8 shows the 3D birds-eye view of the melt surface with the temperature distribution, which is cut on the cross-section in the center of the y-direction, for the same time points as in Fig. 7. The liquid/gas interface strongly fluctuates with the instantaneous keyhole shape just after the powder particles melt, and then gradually flattens. On the other hand, the initial spaces between the powder particles are immediately transformed into spherical pores after melting. The collision between the generated pores and the fluctuated pushed-down surface can be seen more clearly in Fig. 8. Meanwhile, the colliding pores disappear immediately. The remaining pores float and finally go out into atmosphere by buoyancy. It can be clearly seen that the melt pool surface drops as the pores are expelled. The depth and height of the melt pool decrease along with the progression of the solidification with decreasing temperature, as shown in Fig. 7 (column (2)). It is expected that if the pores are trapped in the solid due to rate of the solidification process being faster than the speed of the outflowing pores, the trapped pores will remain as a defect. Under the present process conditions, no trapped pores were seen (Figs. 7 and 8). Thus, the results in Figs. 7 and 8 confirm that the multi-phase formulation for the MLKS of the CAC equation has the ability to precisely track the liquid/gas interface movement by coupling with the MLKS flow calculations.

The velocity vector and grain distribution on the cross-section in the center of the width (y) direction are shown in Fig. 9. Grain color is graded to crystalline angle φ. It can be seen that flow velocity vector distributions are strongly changed by fluctuations of the liquid/gas interface of the melt pool, particularly around the region where the gas pores go out into the atmosphere. Complex flow distributions result for both the melt pool and atmosphere gas region. As previously mentioned, the pores are not trapped in the solidification microstructure as defects. However, some holes generated by pores appear to have remained as bumps on the solidified surface. The epitaxial grain growth from the melt pool bottom with cooling after beam passing can be seen in Fig. 9 just as in Fig. 7 (2).

The growth directions of the upward epitaxial grains are almost vertical with little incline to the beam traveling direction because the leaned angle of the temperature gradient direction for the traveling direction is also small, as shown in Fig. 7 (column (2)). The growth directions are controlled by the temperature gradient around the solid/liquid interface because solute element diffusion simulation is not implemented in this study. The diffusivity of temperature is generally more than one order of magnitude larger than that of a solute element. Therefore, in the present macroscopic simulation, solute element diffusion is considered to be neglected. However, the influence of the interface anisotropy between liquid and grain seems to appear as boundary roughness in the interfaces between solidified grains.

The temperature and liquid phase distributions on the cross-section in x = 250 μm for the traveling direction are shown in Fig. 10. The flow velocity vector and grain distributions on the cross-section in x = 250 μm for the traveling direction are shown in Fig. 11. Panels (a), (b),

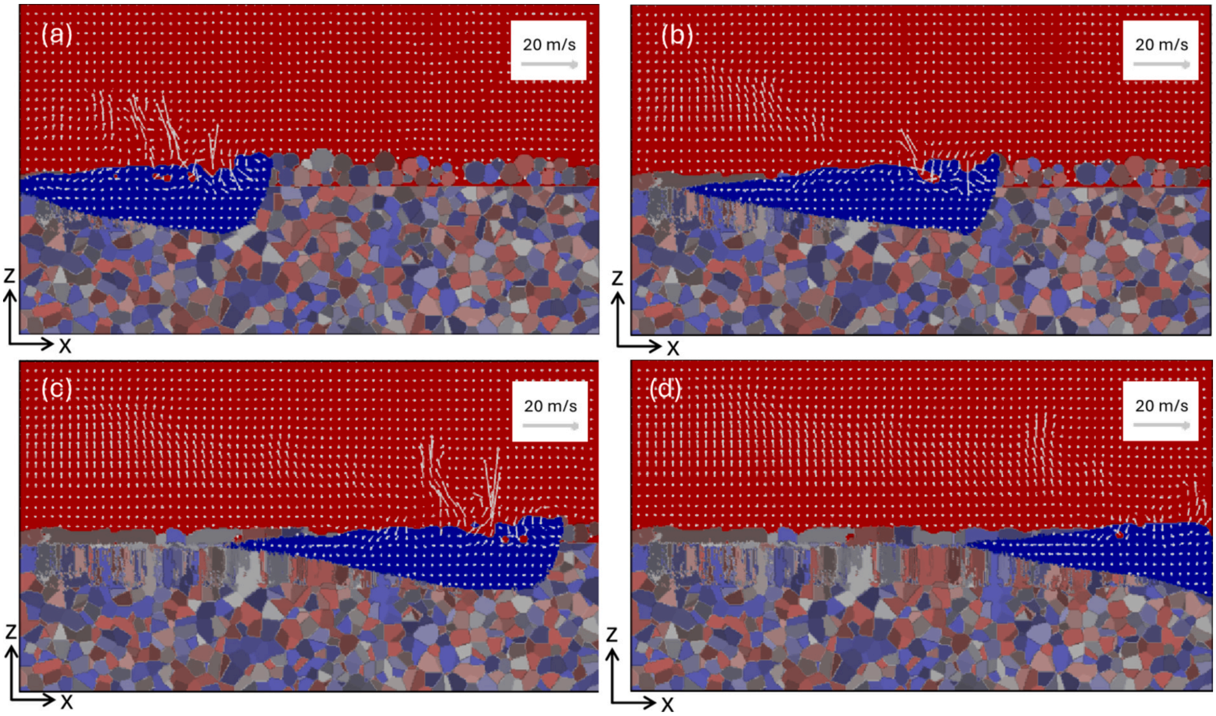

Fig. 9. Flow velocity and grain distributions on a cross-section of the center for the width (y) direction. Red and blue represent the gas and liquid phases, respectively, at (a) 0.4 ms, (b) 0.6 ms, (c) 0.9 ms, and (d) 1.1 ms. (For interpretation of the references to color in this figure legend, the reader is referred to the web version of this article.)

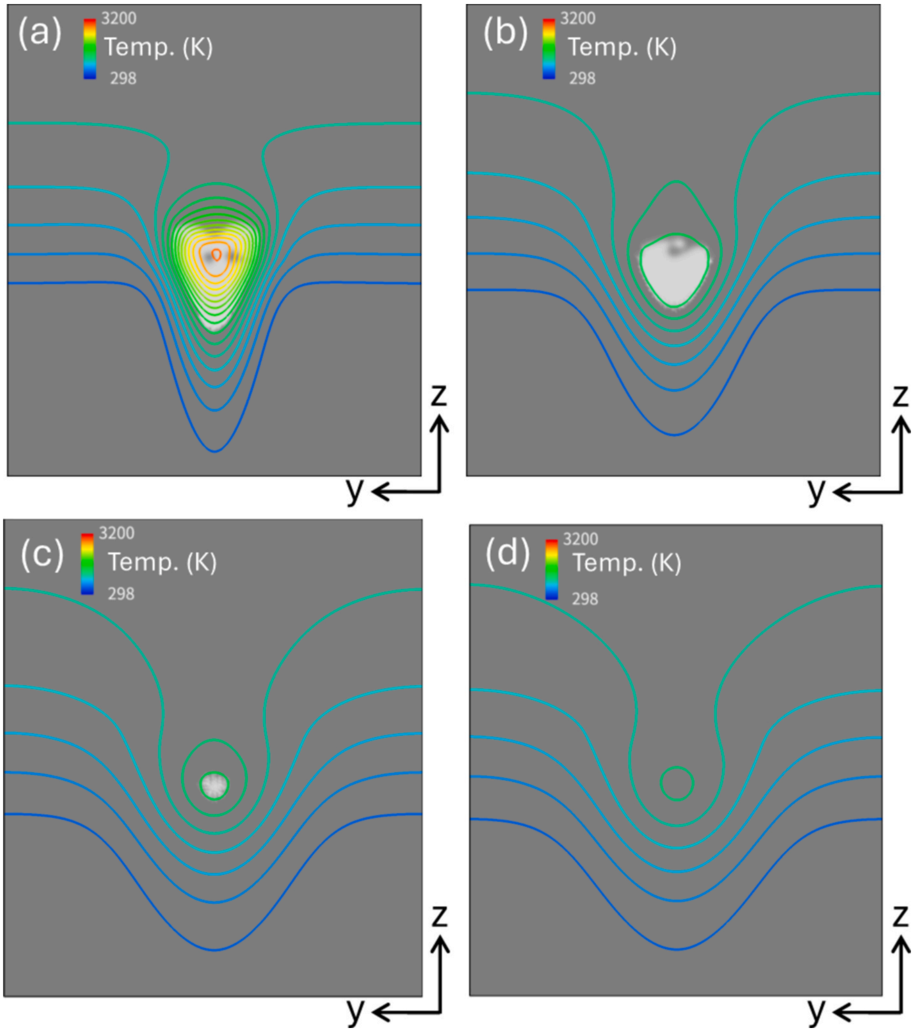

Fig. 10. Temperature and liquid phase distributions on a cross-section in 250 μm for the traveling (x) direction at times (a) 0.3 ms, (b) 0.5 ms, (c) 0.7 ms, and (d) 0.8 ms.

(c) and (d) of Figs. 10 and 11 show the results for the same time points of 0.3, 0.5, 0.7 and 0.8 ms, respectively. It can be seen that the melt pool size of the cross-section is reduced with the maximum temperature values decreasing from (a) to (d) in Fig. 10. Comparing Figs. 10 and 11, it can be seen that the liquid/gas surface drops as from (a) to (b) as the pores are expelled from the melt pool. As the temperature decreases around the melt pool, the epitaxial grains grow from liquid/grain interfaces for the maximum temperature point. Thus, at the bottom of the melt pool, most of the grains grow vertically, as seen in Fig. 11. The powder particles on both sides in the melt pool surface grow horizontally for the center of the melt pool, as seen in panels (b) and (c) in Fig. 11. These morphological tendencies are in qualitative agreement with the experimental measurement in the Ni alloy PBF [29]. In the experimental measurement, an equiaxed microstructure around the liquid/gas surface is often observed. The temperature gradient around the liquid/gas surface is smaller than that in the liquid/solid interface, as seen in panel (a) of Fig. 11. This makes capability for cellular-to-equiaxed transition (CET) around the liquid/gas interface much higher than for the liquid/solid interface. This study did not implement a nucleation model for the equiaxed solidification. We consider that the equiaxed solidification feature is not mandatory for a process in which cellular grain growth is the dominant mechanism because the grain structure around the surface is remelted by beam traveling in the next layer.

The complex flow velocity distribution around the liquid/gas surface is also observed in (a) and (b) in Fig. 10 just as in Fig. 9. Especially, high velocity from the melt pool to the atmosphere occurs where the pores go out into atmosphere as shown in panel (b) of Fig. 11. After the melt pool surface solidifies, gas flow convection remains and rather accelerates above the melt pool area as seen in panels (c) and (d) of Fig. 11. This is considered to be the reason that the symmetrical boundary condition of flow for the simulation region designed in Fig. 6 conserves heated energy, some part of which continues to be transformed to a floating flow region. Conversely, this result confirms that the Boussinesq approximation in Eq. (24) works precisely for the change in density as a function of temperature.

Structural or mechanical parts produced by the LBPF process are severely affected by porosity defects due to the complex melt flow and rapid solidification during fabrication. To improve the quality of the final product, it is necessary to study the mechanisms of pore formation. Many studies have been reported so far by experimental [20–26] or numerical approaches [27–40], as mentioned in the introduction. Based on the present numerical results, the formation mechanism of pore and transformation will be discussed. Before the discussion, it should be noted that the LPBF process causes other defects such as adhesion of unmelted powder particles, balling phenomena, surface and internal cracks, stair-case effect on the part surface and distortion and delamination of the part [22]. In this study, only pore formation is discussed in the limited physical models and process conditions. Furthermore, pores are classified into keyhole pores, powder pores and hydrogen pores. In

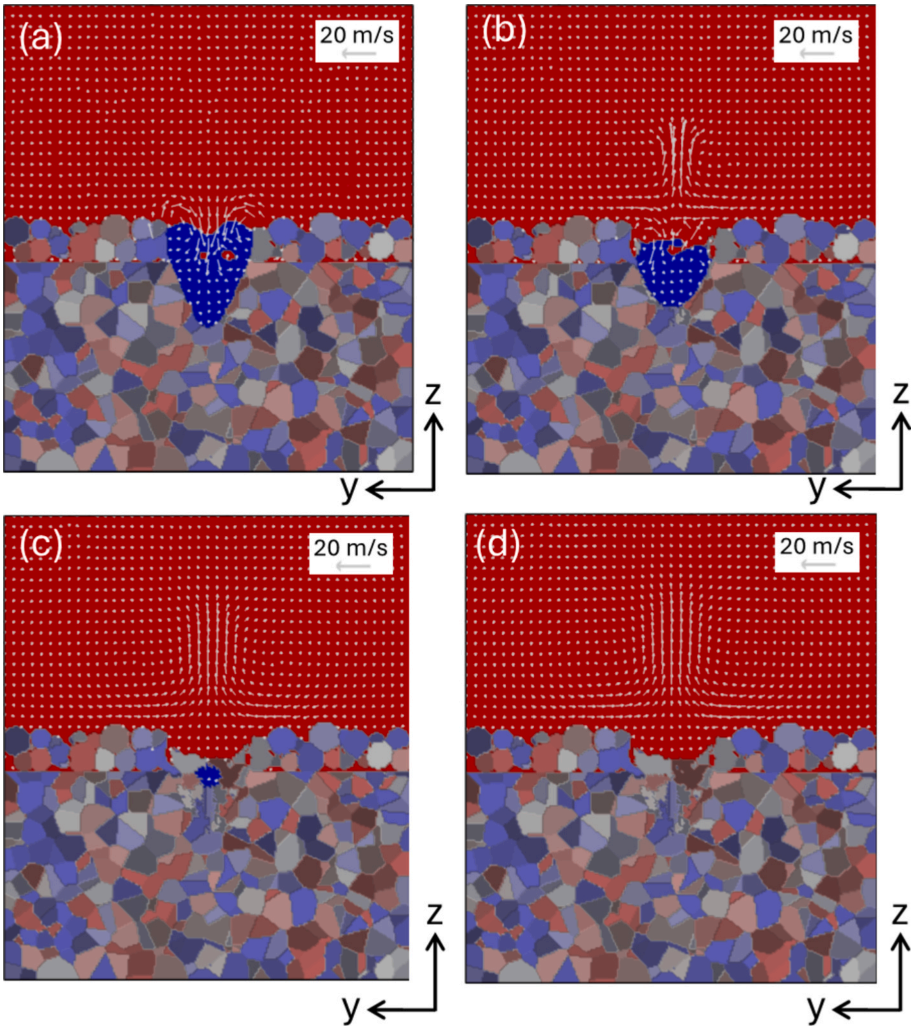

Fig. 11. Flow velocity vector and grain distributions on cross-section in 250 μm for traveling (x) direction at times (a) 0.3 ms, (b) 0.5 ms, (c) 0.7 ms, and (d) 0.8 ms.

this classification, the powder pore is defined as being generated from the initial gas space between powders in this study. The hydrogen pores are known to be common in LPBF processes for Al, Ti and Fe alloys [22]. The hydrogen pores are not treated in this study because of chemical reaction or diffusion is not considered in the simulation model.

Keyhole formations can be clearly seen in Figs. 7, 8, and 9. These mechanisms are explained as follows. First, a melt pool is formed by the laser beam heating the powder and the base plate. At the same time, the molten metal is boiled with a higher energy input and its recoil pressure pushes down the surface of the melt pool surface. If the laser power density is greater than a certain threshold value, which depends on the metal alloy and process parameters [80], the depth of penetration increases as the dip width narrows. The keyhole formation is then established. In addition, the laser density is concentrated by many beam reflections in the narrow keyhole. The keyhole growth appears to continue until the absorbed laser power is consumed. As the down-pressure decreases with the laser power consumption, the free surface in the bottom of the keyhole starts to float by buoyancy. As a result, the gas space around the keyhole bottom becomes spherical due to the interfacial tension between the gas and liquid phases. Finally, the pore is formed by the spherical gas space separated from the keyhole and is transported by the melt pool flow convection and buoyancy. From the previous studies, the keyhole generated pore usually occurs when the keyhole depth is very large, equal to the melt pool bottom depth. As the keyhole pore is usually associated with large defects, the process conditions are designed to avoid it. In this study, the keyhole depth is very small compared to the melt pool depth and any keyhole pore is not confirmed in Figs. 7-9 because the process conditions of the calculation are the same as the practical manufacturing ones.

It is well known that LPBF powders produced by the gas atomization method contain a feedstock porosity of about 0.20 % [81]. However, the influence of the feedstock has not been considered in this discussion because it is not modelled in this study and is relatively small compared to the initial inter-powder space, where the packing ratio is around 45 %. The pores shown in the previous figures are mainly powder pores in the present simulation results. Meanwhile, the keyhole formulations cause strong fluctuation of the melt pool surface motion, as seen in Figs. 7-9 and 11, even when the keyhole depth is small. Although the surface fluctuation motion is strong, it seems to accelerate the flow velocity around the bottom of the melt pool only slightly, as seen in Fig. 9. In other words, the convective flow region of relatively high velocity is restricted in the shallow region from the melt pool surface. Figs. 7-9 show that the powder pores are transported from the surface by the shallow convection flow and disappear from the melt pool surface by buoyancy. The strong fluctuations of the surface are considered to accelerate the disappearance of the powder pore before the solidification interface trapping pores. In Figs. 9 and 11, there are no pore defects in the solidified microstructure region below the initial boundary between the base plate and the powder bed. Some powder defects can be seen in the upper region of the microstructure in Fig. 9 (c) and (d) and Fig. 11 (c) and (d). These defects are not problems because the surface area is remelted after a new powder bed is fed in the practical engineering process. On the other hand, in the high laser power density condition, which can be called “off design” condition, the keyhole pore generated in the deep region of the melt pool is considered to have a tendency to be trapped in the solidification interface because the keyhole pore takes longer time to disappear from the melt pool surface than the powder pore. The present computational method will become a tool to design the appropriate process condition to avoid “off design”.

6. Conclusions

In this study, a modified lattice kinetic scheme, which was a kind of lattice Boltzmann method, was adapted to simulate gas and liquid flows in a 3D model of the laser powder bed fusion process. The multi-phase formulation of the modified lattice kinetic scheme for the conserved Allen–Cahn equation was newly derived to track liquid/gas free surface movement in a three-phase system including a solid phase. The multi-phase field was introduced to evolve the melting and solidification microstructure. These equations were solved by coupling with the thermal equation in the synchronized same time. Simulation for one traveling beam was performed by using an OpenMP/MPI paralleling program developed in-house. The following results were obtained.

(1) It is confirmed that the modified lattice kinetic scheme for calculating liquid and gas flows gives high speed and robustness under the condition of liquid/gas and solid/liquid interface movements by coupling thermal analysis. Especially, the rapidly changing velocity around the fluctuating liquid/gas surface and expulsion of pores were precisely estimated. The time elapsed for one laser traveling length, 1000 μm, was measured as approximately 41 h, including the time spent for solidification microstructure evolution.
(2) The derived multi-phase formulation of the modified lattice kinetic scheme for the conserved Allen–Cahn equation was confirmed to effectively track the liquid/gas free surface movement by coupling with flow in the melt pool. The highly fluctuating surface was pushed down by recoil pressure, which had a keyhole shape, and pore generation from the initial space between powder particles was observed. Consequently, their collisions were also identified. Finally, pores going out into the atmosphere by convective flow affected by buoyancy were also identified.
(3) Melting and solidification are confirmed to be well estimated by using a multi-phase field method coupled with analyses using the thermal equation and the multi-phase equation of the modified lattice kinetic scheme for the conserved Allen–Cahn equation in a system with solid, liquid and gas phases. The solidification direction on the liquid/solid interface was observed to be mainly controlled by the temperature gradient. However, the solidified grain boundary shape seemed to be complex due to the interface anisotropy function implemented in the multi-phase field method.

CRediT authorship contribution statement

Sukeharu Nomoto: Writing – original draft. **Masahiro Kusano:** Validation. **Tomonori Kitashima:** Validation. **Makoto Watanabe:** Writing – review & editing, Funding acquisition.

Declaration of competing interest

The authors declare the following financial interests/personal relationships which may be considered as potential competing interests: [Makoto Watanabe reports financial support was provided by Innovative Science and Technology Initiative for Security. Reports a relationship with that includes:. Has patent pending to. If there are other authors, they declare that they have no known competing financial interests or personal relationships that could have appeared to influence the work reported in this paper].

Acknowledgment

This work was financially supported by a grant from the Innovative Science and Technology Initiative for Security (No. JPJ004596) implemented by the Acquisition, Technology, and Logistics Agency (ATLA) of Japan, and the Amada Foundation (No. AF-2022201-A3), Japan.

Data availability

Data will be made available on request.

References

[1] W.E. Frazier, Metal additive manufacturing: a review, JMEPEG 23 (2014) 1917–1928, https://doi.org/10.1007/s11665-014-0958-z.
[2] B. Blakey-Milner, P. Gradl, G. Snedden, M. Brooks, J. Pitot, E. Lopez, M. Leary, F. Berto, A. du Plessis, Metal additive manufacturing in aerospace: a review, Mater. Des. 209 (2021) 110008, https://doi.org/10.1016/j.matdes.2021.110008.
[3] A. Vafadar, F. Guzzomi, A. Rassau, K. Hayward, Advances in metal additive manufacturing: a review of common processes, industrial applications, and current challenges, Appl. Sci. 11 (2021) 1213, https://doi.org/10.3390/app11031213.
[4] V. Dhinakaran, J. Ajith, A. Fathima Yasin Fahmidha, T. Jagadeesha, T. Sathish, B. Stalin, Wire Arc Additive Manufacturing (WAAM) process of nickel based superalloys – a review, Mater. Today Proc. 21 (2020) 920–925, https://doi.org/10.1016/j.matpr.2019.08.159.
[5] Y. Li, C. Su, J. Zhu, Comprehensive review of wire arc additive manufacturing: hardware system, physical process, monitoring, property characterization, application and future prospects, Results Eng. 13 (2022) 100330, https://doi.org/10.1016/j.rineng.2021.100330.
[6] M. Srivastava, S. Rathee, A. Tiwari, M. Dongre, Wire arc additive manufacturing of metals: a review on processes: materials and their behaviour, Mater. Chem. Phys. 294 (2023) 126988, https://doi.org/10.1016/j.matchemphys.2022.126988.
[7] M. Liu, A. Kumar, S. Bukkapatnam, M. Kuttolamadom, A review of the anomalies in Directed Energy Deposition (DED) processes & potential solutions - part quality & defects, Procedia Manuf. 53 (2021) 507–518, https://doi.org/10.1016/j.promfg.2021.06.093.
[8] D. Svetlizky, M. Das, B. Zheng, A.L. Vyatskikh, S. Bose, A. Bandyopadhyay, J. M. Schoenung, E.J. Lavernia, N. Eliaz, Directed energy deposition (DED) additive manufacturing: physical characteristics, defects, challenges and applications, Mater. Today 49 (2021) 271–295, https://doi.org/10.1016/j.mattod.2021.03.020.
[9] D. -Gyu Ahn, Directed Energy Deposition (DED) process: state of the art, Inter. J. Precis. Engineer. Manuf.-Green Tech. 8 (2021) 703–742, https://doi.org/10.1007/s40684-020-00302-7.
[10] A. Mostafaei, A.M. Elliott, J.E. Barnes, F. Li, W. Tan, C.L. Cramer, P. Nandwana, M. Chmielus, Binder jet 3D printing—process parameters, materials, properties, modeling, and challenges, Prog. Mater Sci. 119 (2021) 100707, https://doi.org/10.1016/j.pmatsci.2020.100707.
[11] X. Chen, S. Wang, J. Wu, S. Duan, X. Wang, X. Hong, X. Han, C. Li, D. Kang, Z. Wang and A. Zheng, The Application and Challenge of Binder Jet 3D Printing Technology in Pharmaceutical Manufacturing, *pharmaceutics* 2022, 14, 2589. DOI: 10.3390/pharmaceutics14122589.
[12] H.R. Kotadia, G. Gibbons, A. Das, P.D. Howes, A review of Laser powder bed fusion additive manufacturing of aluminum alloys: microstructure and properties, Addit. Manuf. 46 (2021) 102155, https://doi.org/10.1016/j.addma.2021.102155.
[13] S. Sanchez, P. Smith, Z. Xu, G. Gaspard, C.J. Hyde, W.W. Wits, I.A. Ashcroft, H. Chen, A.T. Clare, Powder Bed Fusion of nickel-based superalloys: A review,Int, J. Mach. Tool Manu 165 (2021) 103729, https://doi.org/10.1016/j.ijmachtools.2021.103729.
[14] S. Chowdhury, N. Yadaiah, C. Prakash, S. Ramakrishna, S. Dixit, L. Raj Gupta, D. Buddhi, Laser powder bed fusion: a state-of-the-art review of the technology, materials, properties & defects, and numerical modelling, J. Mater. Research and Technol. 20 (2022) 2109–2172, https://doi.org/10.1016/j.jmrt.2022.07.121.
[15] G. Maziero Volpato, U. Tetzlaff, M. Celso Fredel, A comprehensive literature review on laser powder bed fusion of Inconel superalloys, Addit. Manuf. 55 (2022) 102871, https://doi.org/10.1016/j.addma.2022.102871.
[16] M.H. Farshidianfar, A. Khajepour, A.P. Gerlich, Effect of real-time cooling rate on microstructure in Laser Additive Manufacturing, J. Mater. Process. Technol. 231 (2016) 468–478, https://doi.org/10.1016/j.jmatprotec.2016.01.017.
[17] U.S. Bertoli, G. Guss, S. Wu, M.J. Matthews, J.M. Schoenung, In-situ characterization of laser-powder interaction and cooling rates through high-speed imaging of powder bed fusion additive manufacturing, Mater. Des. 135 (2017) 385–396, https://doi.org/10.1016/j.matdes.2017.09.044.
[18] V. Thampy, A.Y. Fong, N.P. Calta, J. Wang, A. Martin, P.J. Depond, A.M. Kiss, G. Guss, Q. Xing, R.T. Ott, A. van Buuren, M.F. Toney, J.N. Weker, M.J. Kramer, M. J. Matthews, C.J. Tassone1, K.H. Stone, Subsurface cooling rates and microstructural response during laser based metal additive manufacturing, *Sci. Rep.* 1981 (2020) 10, https://doi.org/10.1038/s41598-020-58598-z.

[19] S. Nomoto, M. Segawa, M. Watanabe, Non- and Quasi-equilibrium multi-phase field methods coupled with CALPHAD database for rapid-solidification microstructural evolution in laser powder bed additive manufacturing condition, Metals 11 (2021) 626, https://doi.org/10.3390/met11040626.

[20] E. Li, Z. Zhou, L. Wang, H. Shen, R. Zou, A. Yu, Particle scale modeling of melt pool dynamics and pore formation in selective laser melting additive manufacturing, Powder Technol. 397 (2022) 117012, https://doi.org/10.1016/j.powtec.2021.11.056.

[21] V. Subraveti, B. Richter, S.R. Yeratapally, C. Oskay, Three-dimensional prediction of lack-of-fusion porosity volume fraction and morphology for powder bed fusion additively manufactured Ti–6Al–4V, Integrating Materials and Manufacturing Innovation 13 (2024) 511–525, https://doi.org/10.1007/s40192-024-00347-5.

[22] C. Du, Y. Zhao, J. Jiang, Q. Wang, H. Wang, N. Li, J. Sun, Pore defects in laser powder bed fusion: formation mechanism, control method, and perspectives, J. Alloy. Compd. 944 (2023) 169215, https://doi.org/10.1016/j.jallcom.2023.169215.

[23] J.P. Oliveira, A.D. LaLonde, J. Mac, Processing parameters in laser powder bed fusion metal additive manufacturing, Mater. Des. 193 (2020) 108762, https://doi.org/10.1016/j.matdes.2020.108762.

[24] S. Feng, Z. Chen, B. Bircher, Z. Ji, L. Nyborg, S. Bigot, Predicting laser powder bed fusion defects through in-process monitoring data and machine learning, Mater. Des. 222 (2022) 111115, https://doi.org/10.1016/j.matdes.2022.111115.

[25] Q. Liu, H. Wu, M.J. Paul, P. He, Z. Peng, B. Gludovatz, J.J. Kruzic, C.H. Wang, X. Li, Machine-learning assisted laser powder bed fusion process optimization for AlSi10Mg: new microstructure description indices and fracture mechanisms, Acta Mater. 201 (2020) 316–328, https://doi.org/10.1016/j.actamat.2020.10.010.

[26] X. Qi, G. Chen, Y. Li, X. Cheng, C. Li, Applying neural-network-based machine learning to additive manufacturing: current applications perspectives, Challenges, and Future Eng. 5 (2019) 721–729, https://doi.org/10.1016/j.eng.2019.04.012.

[27] P. Scheel, R. Wrobel, B. Rheingans, T. Mayer, C. Leinenbach, E. Mazza, E. Hosseini, Advancing efficiency and reliability in thermal analysis of laser powder-bed fusion, Int. J. Mech. Sci. 260 (2023) 108583, https://doi.org/10.1016/j.ijmecsci.2023.108583.

[28] E. Hosseinia, P. Scheela, O. Müllera, R. Molinaroc, S. Mishrad, Single-track thermal analysis of laser powder bed fusion process: parametric solution through physics-informed neural networks, Comput. Methods Appl. Mech. Engrg. 410 (2023) 116019, https://doi.org/10.1016/j.cma.2023.116019.

[29] M. Kusano, M. Watanabe, Heat source model development for thermal analysis of laser powder bed fusion using bayesian optimization and machine learning, Integrating Materials and Manufacturing Innovation 13 (2024) 288–304, https://doi.org/10.1007/s40192-023-00334-2.

[30] Z. Luo, Y. Zhao, A survey of finite element analysis of temperature and thermal stress fields in powder bed fusion additive manufacturing, Addit. Manuf. 21 (2018) 318–332, https://doi.org/10.1016/j.addma.2018.03.022.

[31] Z.-J. Li, H.-L. Dai, Y. Yao, J.-L. Liu, A semi-analytical model for rapid prediction of residual stress and deformation in laser powder bed fusion, App. Math. Model. 125 (2024) 672–686, https://doi.org/10.1016/j.apm.2023.10.024.

[32] Yu. Zhen Chen, Z.W. Xiang, P. Wei, Lu. Bingheng, L. Zhang, Du. Jun, Thermal dynamic behavior during selective laser melting of K418 superalloy: numerical simulation and experimental verification, Appl. Phys. A 124 (2018) 313, https://doi.org/10.1007/s00339-018-1737-8.

[33] S. Mohammad, H. Hojjatzadeh, N.D. Parab, W. Yan, Q. Guo, L. Xiong, C. Zhao, M. Qu, L.I. Escano, X. Xiao, K. Fezzaa, W. Everhart, T. Sun, L. Chen, Pore elimination mechanisms during 3D printing of metals, Nature Communications 10 (2019) 3088, https://doi.org/10.1038/s41467-019-10973-9.

[34] C. Panwisawas, B. Perumal, R.M. Ward, N. Turner, R.P. Turner, J.W. Brooks, H. C. Basoalto, Keyhole formation and thermal fluid flow-induced porosity during laser fusion welding in titanium alloys: experimental and modelling, Acta. Mater. 126 (2017) 251–263, https://doi.org/10.1016/j.actamat.2016.12.062.

[35] Chunlei Qiu, Chinnapat Panwisawas, Mark Ward, Hector C. Basoalto, Jeffery W. Brooks, Moataz M. Attallah, On the role of melt flow into the surface structure and porosity development during selective laser melting, Acta Mater. 96 (2015) 72–79, https://doi.org/10.1016/j.actamat.2015.06.004.

[36] Y. Chen, Y. Wang, H. Li, Y. Lu, B. Han, Q. Zhang, Effects of process parameters on the microstructure of Inconel 718 during powder bed fusion based on cellular automata approach, Virtual and Physical Prototyping 18 (2023) e2251032, https://doi.org/10.1080/17452759.2023.2251032.

[37] Y. Zhanga, J. Zhanga, Modeling of solidification microstructure evolution in laser powder bed fusion fabricated 316L stainless steel using combined computational fluid dynamics and cellular automata, Addit. Manuf. 28 (2019) 750–765, https://doi.org/10.1016/j.addma.2019.06.024.

[38] H. Azizi, A. Ebrahimi, N. Ofori-Opoku, M. Greenwood, N. Provatas, M. Mohammadi, Characterizing the microstructural effect of build direction during solidification of laser-powder bed fusion of Al-Si alloys in the dilute limit: a phase-field study, Acta Mater. 214 (2021) 116983, https://doi.org/10.1016/j.actamat.2021.116983.

[39] S.M. Elahi, R. Tavakoli, A.K. Boukellal, T. Isensee, I. Romero, D. Tourret, Multiscale simulation of powder-bed fusion processing of metallic alloys, Comput. Mater. Sci 209 (2022) 111383, https://doi.org/10.1016/j.commatsci.2022.111383.

[40] J. Shinjo, A. Kutsukake, A. Arote, Y.T. Tang, D.G. McCartney, R.C. Reed, C. Panwisawas, Physics-based thermal-chemical-fluid-microstructure modelling of in-situ alloying using additive manufacturing: composition-microstructure control, Addit. Manuf. 64 (2023) 103428, https://doi.org/10.1016/j.addma.2023.103428.

[41] X. Zhang, H. Wang, W. Kuang, J. Zhang, Application of the thermodynamic extremal principle to phase-field modeling of non-equilibrium solidification in multi-component alloys, Acta Mater. 128 (2017) 258e269, https://doi.org/10.1016/j.actamat.2017.02.026.

[42] K. Karayagiz, L. Johnson, R. Seede, V. Attari, B. Zhang, X. Huang, S. Ghosh, T. Duong, I. Karaman, A. Elwany, R. Arróyave, Finite interface dissipation phase field modeling of Ni–Nb under additive manufacturing conditions, Acta Mater. 185 (2020) 320–339, https://doi.org/10.1016/j.actamat.2019.11.057.

[43] J. Katagiri, S. Nomoto, M. Kusano, M. Watanabe, Particle size effect on powder packing properties and molten pool dimensions in laser powder bed fusion simulation, J. Manuf. Mater. Process. 8 (2024) 71, https://doi.org/10.3390/jmmp8020071.

[44] R. Zhang, X. He, S. Chen, Interface and surface tension in incompressible lattice Boltzmann multiphase model, Comput. Phys. Commun. 129 (2000) 121–130, https://doi.org/10.1016/S0010-4655(00)00099-0.

[45] X. He, S. Chen, R. Zhang, A lattice boltzmann scheme for incompressible multiphase flow and its application in simulation of rayleigh–taylor instability, J. Comput. Phys. 152 (1999) 642–663, https://doi.org/10.1006/jcph.1999.6257.

[46] A. Rai, M. Markl, C. Körner, A coupled Cellular Automaton–Lattice Boltzmann model for grain structure simulation during additive manufacturing, Comput. Mater. Sci 124 (2016) 37–48.

[47] M. Zheng, G. Wang, W. Zhou, L. Wei, X. Lin, W. Huang, Understanding grain evolution in laser powder bed fusion process through a real-time coupled Lattice Boltzmann model-Cellular Automaton simulation, J. Materials Processing Tech. 321 (2023) 118126, https://doi.org/10.1016/j.jmatprotec.2023.118126.

[48] C.W. Hirt, B.D. Nichols, Volume of Fluid (VOF) method for the dynamics of free boundaries, J. Comput. Phys. 39 (1981) 201–225.

[49] W. Zhang, D. Sun, W. Chen, S. Chen, Lattice Boltzmann modeling of convective heat and solute transfer in additive manufacturing of multi-component alloys, Addit. Manuf. 84 (2024) 104089, https://doi.org/10.1016/j.addma.2024.104089.

[50] Q. Li, K.H. Luo, Q.J. Kang, Y.L. He, Q. Chen, Q. Liu, Lattice Boltzmann methods for multiphase flow and phase-change heat transfer, Prog. Energy Combust. Sci. 52 (2016) 62–105, https://doi.org/10.1016/j.pecs.2015.10.001.

[51] H. Liang, Z.H. Chai, B.C. Shi, Z.L. Guo, T. Zhang, Phase-field-based lattice Boltzmann model for axisymmetric multiphase flows, Phys. Rev. E 90 (2014) 063311, https://doi.org/10.1103/PhysRevE.90.063311.

[52] L. Zheng, S. Zheng, Q. Zhai, Lattice Boltzmann equation method for the Cahn-Hilliard equation, Phys. Rev. E 91 (2015) 013309, https://doi.org/10.1103/RhysRevE.91.013309.

[53] N. Takada, J. Matsumoto, S. Matsumoto, K. Kurihara, Phase-field model-based simulation of two-phase fluid motion on partially wetted and textured solid surface, J. Computational Sci. 17 (2016) 315–324, https://doi.org/10.1016/j.jocs.2016.05.009.

[54] C. Schwarzmeier, M. Holzer, T. Mitchell, M. Lehmann, F. Häusl, U. Rüde, Comparison of free-surface and conservative Allen-Cahn phase-field lattice Boltzmann method, J. Comput. Phys. 473 (2023) 111753, https://doi.org/10.1016/j.jcp.2022.111753.

[55] P. Yue, C. Zhou, J.J. Feng, Spontaneous shrinkage of drops and mass conservation in phase-field simulations, J. Comput. Phys. 223 (2007) 1–9, https://doi.org/10.1016/j.jcp.2006.11.020.

[56] T. Inamuro, A lattice kinetic scheme for incompressible viscous flows with heat transfer, Phil. Trans. R. Soc. Lond. A 360 (2002) 477–484, https://doi.org/10.1098/rsta.2001.0942.

[57] T. Inamuro, T. Echizen, F. Horai, Validation of an improved lattice Boltzmann method for incompressible two-phase flows, Comput. Fluids 175 (2018) 83–90, https://doi.org/10.1016/j.compfluid.2018.08.017.

[58] H.G. Lee, J. Kim, An efficient numerical method for simulating multiphase flows using a diffuse interface model, Phys. A 423 (2015) 33–50, https://doi.org/10.1016/j.physa.2014.12.027.

[59] I. Steinbach, Phase-field models in materials science, Modelling Simul. Mater. Sci. Eng. 17 (2009) 073001, https://doi.org/10.1088/0965-0393/17/7/073001.

[60] T. Kruger, H. Kusumaatmaja, A. Kuzmin, O. Shardt, G. Silva, The Lattice Boltzmann Method, Graduate Texts in Physics, Springer International Publishing AG Switzerland, 2017, pp. 86–92.

[61] T. Inamuro, M. Yoshino, K. Suzuki, An Introduction to the Lattice Boltzmann Mehod, Maruzen, World Scientific publishing, 2022, pp. 89–90.

[62] J.U. Brackbill, D.B. Kothe, C. Zemach, A continuum method for modeling surface tension, J. Comput. Phys. 100 (1992) 335–354, https://doi.org/10.1016/0021-9991(92)90240-Y.

[63] S.I. Anisimov, V.A. Khokhlov, Instabilities in Laser-matter Interaction, CRC, Boca Raton, Fl, 1996. doi: 10.1017/S0263034600010491.

[64] S.A. Khairallah, A.T. Anderson, A. Rubenchik, W.E. King, Laser powder-bed fusion additive manufacturing: physics of complex melt flow and formation mechanisms of pores, spatter, and denudation zones, Acta Mater. 108 (2016) 36–45, https://doi.org/10.1016/j.actamat.2016.02.014.

[65] H.K. Lin, C.C. Chen, C.W. Lan, Adaptive three-dimensional phase-field modeling of dendritic crystal growth with high anisotropy, J. Cryst. Growth 318 (2011) 51–54, https://doi.org/10.1016/j.jcrysgro.2010.11.013.

[66] C.J. Knight, Theoretical modeling of rapid surface vaporization with back pressure, AIAA J. 17 (1979) 78–1220, https://doi.org/10.2514/3.61164.

[67] Numerical Materials Simulator Station of the National Institute for Materials Science, https://home.nims.go.jp/supercom/new/index_e.htm (Accessed 09 January).

[68] B. Stump, A. Plotkowski, Spatiotemporal parallelization of an analytical heat conduction model for additive manufacturing via a hybrid OpenMP + MPI approach, Comput. Mater. Sci. 184 (2020) 109861, https://doi.org/10.1016/j.commatsci.2020.109861.

[69] J. Kim, A generalized continuous surface tension force formulation for phase-field models for multi-component immiscible fluid flows, Comput. Methods Appl. Mech. Eng. 198 (37–40) (2009) 3105–3112, https://doi.org/10.1016/j.cma.2009.05.008.

[70] F. Boyer, C. Lapuerta, S. Minjeaud, B. Piar, M. Quintard, Cahn–hilliard/navier–stokes model for the simulation of three-phase flows, Transp. Porous Media 82 (2010) 463–483.

[71] S. Aihara, T. Takaki, N. Takada, Multi-phase-field modeling using a conservative Allen–Cahn equation for multiphase flow, Comput. Fluids 178 (2019) 141–151, https://doi.org/10.1016/j.compfluid.2018.08.023.

[72] M. Imaran, J. Young, R. Capozza, K. Stratford, K.J. Hanley, Spherical harmonic–based DEM in LAMMPS: implementation, verification and performance assessment, Comput. Phys. Commun. 304 (2024) 109290, https://doi.org/10.1016/j.cpc.2024.109290.

[73] D. Gründing, M. Smuda, T. Antritter, M. Fricke, D. Rettenmaier, F. Kummer, P. Stephan, H. Marschall, D. Bothe, A comparative study of transient capillary rise using direct numerical simulations, App. Math. Model. 86 (2020) 142–165, https://doi.org/10.1016/j.apm.2020.04.020.

[74] CALPHAD Software, https://thermocalc.com/products/thermo-calc/ (Accessed 29 Novenber)).

[75] D. Grange, A. Queva, G. Guillemot, M. Bellet, J.-D. Bartout, C. Colin, Effect of processing parameters during the laser beam melting of Inconel 738: comparison between simulated and experimental melt pool shape, J. Mater. Process. Technol. 289 (2021) 116897, https://doi.org/10.1016/j.jmatprotec.2020.116897.

[76] K.C. Mills, Y.M. Youssef, Z. Li, Y. Su, Calculation of thermophysical properties of ni-based superalloys, ISIJ Int. 46 (2006) 623–632.

[77] P.N. Quested, R.F. Brooks, L. Chapman, R. Morrell, Y. Youssef, K.C. Mills, Measurement and estimation of thermophysical properties of nickel based superalloys, Mater. Sci. Technol. 25 (2009) 154–162, https://doi.org/10.1179/174328408X361454.

[78] J. Katagiri, M. Kusano, S. Nomoto, M. Watanabe, Influence of recoil pressure, mushy zone flow resistance and reflectivity on melt pool shape in laser powder bed fusion simulation, Case Studies in Thermal Eng. 50 (2023) 103477, https://doi.org/10.1016/j.csite.2023.103477.

[79] M. Moda, A. Chiocca, G. Macoretta, B.D. Monelli, L. Bertini, Technological implications of the Rosenthal solution for a moving point heat source in steady state on a semi-infinite solid, Mater. Des. 223 (2022) 110991, https://doi.org/10.1016/j.matdes.2022.110991.

[80] R. Cunningham, C. Zhao, N. Parab, C. Kantzos, J. Pauza, K. Fezzaa, T. Sun, A. D. Rollett, Keyhole threshold and morphology in laser melting revealed by ultrahigh-speed X-ray imaging, Sci. 363 (6429) (2019) 849–852, https://doi.org/10.1126/science.aav4687.

[81] G. Chen, S.Y. Zhao, P. Tan, J. Wang, C.S. Xiang, H.P. Tang, A comparative study of Ti-6Al-4V powders for additive manufacturing by gas atomization, plasma rotating electrode process and plasma atomization, Powder Technol. 333 (2018) 38–46, https://doi.org/10.1016/j.powtec.2018.04.013.